UNCLASSIFIED

AD NUMBER
ADB392010

LIMITATION CHANGES

TO:

Approved for public release; distribution is unlimited.

FROM:

Distribution authorized to U.S. Gov't. agencies and their contractors; Critical Technology; FEB 2013. Other requests shall be referred to Director, Edgewood Chemical Biological Center, Attn: RDCB-DRF-T, Aberdeen Proving Ground, MD 21010-5424. This document contains export-controlled technical data.

AUTHORITY

ECBC memo dtd 27 Aug 2014

THIS PAGE IS UNCLASSIFIED

EDGEWOOD CHEMICAL BIOLOGICAL CENTER

U.S. ARMY RESEARCH, DEVELOPMENT AND ENGINEERING COMMAND

Aberdeen Proving Ground, MD 21010-5424

RADIATIVE TRANSFER MODEL FOR CONTAMINATED ROUGH SURFACES

Avishai Ben-David

RESEARCH AND TECHNOLOGY DIRECTORATE

Charles E. Davidson

SCIENCE AND TECHNOLOGY CORPORATION
Edgewood, MD 21040-2734

February 2013

U.S. ARMY
RDECOM

Disclaimer

The findings in this report are not to be construed as an official Department of the Army position unless so designated by other authorizing documents.

REPORT DOCUMENTATION PAGE		*Form Approved* *OMB No. 0704-0188*

1. REPORT DATE *(DD-MM-YYYY)* XX-02-2013	2. REPORT TYPE Final Technical Report	3. DATES COVERED *(From - To)* January 2012 - September 2012

4. TITLE AND SUBTITLE
Radiative Transfer Model for Contaminated Rough Surfaces

5a. CONTRACT NUMBER

5b. GRANT NUMBER

5c. PROGRAM ELEMENT NUMBER

6. AUTHOR(S)
Avishai Ben-David (ECBC) and Charles E. Davidson (STC)

5d. PROJECT NUMBER

5e. TASK NUMBER

5f. WORK UNIT NUMBER

7. PERFORMING ORGANIZATION NAME(S) AND ADDRESS(ES)
Director, ECBC, ATTN: RDCB-DRD-P, APG, MD 21010-5424
STC, 500 Edgewood Road, STE 205, Edgewood, MD 21040-2734

8. PERFORMING ORGANIZATION REPORT NUMBER

ECBC-TR-1084

9. SPONSORING / MONITORING AGENCY NAME(S) AND ADDRESS(ES)
U.S. Army Edgewood Chemical Biological Center, Aberdeen Proving Ground, MD 21010-5424

10. SPONSOR/MONITOR'S ACRONYM(S)
ECBC

11. SPONSOR/MONITOR'S REPORT NUMBER(S)

12. DISTRIBUTION / AVAILABILITY STATEMENT
Approved for public release; distribution unlimited.

13. SUPPLEMENTARY NOTES

14. ABSTRACT
We studied the radiative transfer and reflectance of potassium chlorate and ammonium nitrate contaminated surfaces in mid-wavelength and long-wavelength infrared for detection. Our framework is a combination of theoretical-based radiative transfer (conservation of energy), an empirical approximation for reflectance of rough surfaces, and empirical modifications of the target absorption coefficients to account for effects of deposition morphology. Our model is formulated such that two-way attenuation (by absorption) through the target material is the primary source for spectral features to appear in the observed radiance. We obtained excellent or good results for lab measurements of potassium chlorate on most aluminum surfaces; however, ammonium nitrate on painted aluminum was more complicated due to spectral correlation between compound and surface. Most of the signal energy came from the specular direction, hence, the ability of the model to explain off-specular reflection is of lower importance. Good specificity was demonstrated against lab data (low probability to misidentify potassium chlorate as ammonium nitrate and vice versa). We also observed moderate success on field data.

15. SUBJECT TERMS
radiative transfer, reflectance, rough surface, BRDF, Kramers-Kronig, penetration depth, fill factor, infrared, LWIR, MWIR, absorption coefficient, scattering, potassium chlorate, ammonium nitrate, off-specular, deposition morphology

16. SECURITY CLASSIFICATION OF:			17. LIMITATION OF ABSTRACT	18. NUMBER OF PAGES	19a. NAME OF RESPONSIBLE PERSON Avishai Ben-David
a. REPORT	b. ABSTRACT	c. THIS PAGE			19b. TELEPHONE NUMBER *(include area code)*
U	U	U	UU	62	(410) 436-6631

Standard Form 298 (Rev. 8-98)
Prescribed by ANSI Std. Z39.18

Blank

PREFACE

The work described in this report was authorized under the Army Technology Objective "Detection of Unknown Bulk Explosives." This work was started in January 2012 and completed in September 2012.

The use of either trade or manufacturers' names in this report does not constitute an official endorsement of any commercial products. This report may not be cited for purposes of advertisement.

The text of this report is published as received and was not edited by the Technical Releases Office, U.S. Army Edgewood Chemical Biological Center.

This report has been approved for public release.

Blank

TABLE OF CONTENTS

LIST OF FIGURES

LIST OF TABLES

ACRONYMS

BRDF	Bidirectional Reflectance Distribution Function
MWIR	Mid-Wavelength Infrared
LWIR	Long Wavelength Infrared
pdf	Probability Density Function
rms	root mean squared
KBr	potassium bromide
LOS	line-of-sight
1D	one dimensional
IR	infrared

ABSTRACT

We studied the radiative transfer and reflectance of potassium chlorate and ammonium nitrate contaminated surfaces in mid-wavelength infrared and long wavelength infrared as a first important step for solving the detection problem. Our framework is a combination of theoretical-based radiative transfer (conservation of energy), an empirical approximation for reflectance of rough surfaces, and empirical modifications of the target absorption coefficients to account for effects of deposition morphology. Our model is formulated such that two-way attenuation (by absorption) through the target material is the primary source for spectral features to appear in the observed radiance. We obtained excellent results for lab measurements of potassium chlorate on rough aluminum, painted aluminum, and an aluminum mirror; good results were also obtained for ammonium nitrate on rough aluminum. Ammonium nitrate on painted aluminum was more complicated due to spectral correlation between ammonium nitrate features and the polymer-coated painted aluminum. Most of the signal energy came from the specular direction, hence, the ability of the model to explain off-specular reflection is of lower importance. Good specificity was demonstrated against lab data (low probability to misidentify potassium chlorate as ammonium nitrate and vice versa). We observed moderate success on field data.

RADIATIVE TRANSFER MODEL FOR CONTAMINATED ROUGH SURFACES

1.   INTRODUCTION

The subject of scattering and reflectivity off rough surfaces appears in diverse applications such as radar measurements (e.g., reflectivity of sea surfaces) and quality control of manufacturing optical surfaces used in different instruments. An extensive literature review (171 references) on Bidirectional Reflectance Distribution Function (BRDF) is given by Asmail[1]. Information on scattering theories for scattering from rough surfaces can be found in basic text books[2-6]. In our project we are interested in scattering off rough surfaces in the presence and absence of chemical contamination, which is a subject that is of fundamental importance for developing a technology capable of detecting the presence of residues of explosive material on various surfaces that in general may be considered "rough". Hence, the objective is to enable the detection of contaminated surfaces and furthermore to identify the contamination. In practical applications the contamination may also contain morphology (e.g., spots, irregularities) which makes it a "rough surface" even if the underlying substrate is perfectly smooth.

In this work, we studied the radiative transfer and reflectance of potassium chlorate and ammonium nitrate contaminated surfaces (or substrates). The wavelength region in this study is in mid-wavelength infrared (MWIR) and long wavelength infrared (LWIR). We studied various types of measurements in an increasing level of difficulty. We started with a lab experiment for potassium chlorate and ammonium nitrate (at 50 and 100 µg/cm2) deposited on a rough aluminum surface (off-the-shelf brushed aluminum from Home Depot). The incident radiation in the lab was directional and known; the optical constants of aluminum are available in the literature. Then, we progressed to potassium chlorate and ammonium nitrate deposited on a painted aluminum surface where the optical constants of the painted aluminum are not known and contain absorption features (i.e., it is not spectrally as "flat" as the bare rough aluminum). Finally, we progressed to field data where the deposited potassium chlorate target is illuminated by diffuse atmospheric sky radiance. In the field experiment, we studied a black surface (very low reflectivity) and rough aluminum which was coated (unfortunately) with a polymer that looked spectrally similar to potassium chlorate. In addition we studied a perfectly smooth surface (aluminum mirror) contaminated with potassium chlorate in order to investigate the effect of deposition morphology.

We illustrate the scenario of a contaminated surface illuminated by directional incident radiation (incident angle, θ_i) in Figure 1. This scenario models our lab experiments. The main components of the radiance reflected from the contaminated surface are shown with three bundles of rays, where the longest ray in each bundle identifies the specular direction (where the angle of reflection, θ, is equal to the angle of incidence, $\theta = \theta_i$) and the remaining rays represent all other reflected directions (the diffuse reflectance). In red, we show the reflectance of the bare rough surface, $R_0(\theta)$; in blue, the reflectance of the target's surface; and in green, the reflectance for the photons that interacted with the target's volume. Two types of contributions are included within the target's volume effect: (a) attenuation of incident photons by two-way transmission through the deposited material to and from the underlying surface, and (b) re-direction of incident photons via scattering within the target's volume (some of these photons interact with the rough surface and some do not; all are subject to some level of attenuation due to absorption by the target's volume). The second contribution involves a complicated function (known in radiative transfer as the "phase function") of the material morphology (particle size, shape) and also depends on the optical properties of the material. In our study, we will only

2

explicitly address the first contribution (two-way transmission) of the target volume term. Multiple reflections between the target and the surface are not shown. In our radiative transfer model (Sections 3 and 4) we only account for the transmission volume effect and we neglect scattering within the target as well as multiple reflections between the target and the bare rough surface.
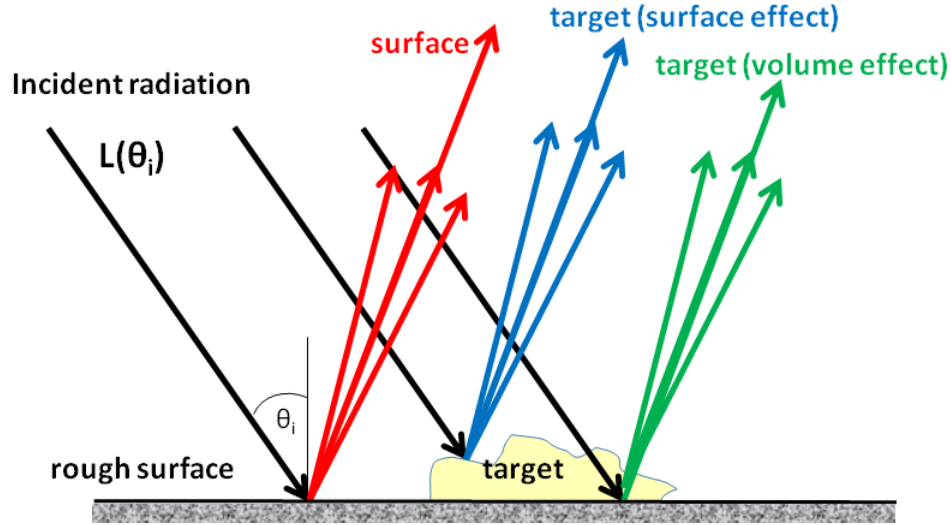
Figure 1. Schematic representation of the radiance components from a contaminated rough surface. In black, the incident radiation $L(\theta_i)$ at direction θ_i; in red, reflectance $R_S(\theta)$ of the rough surface where the longest ray represents the specular direction (at $\theta = \theta_i$) and the other rays represent diffuse reflectance; in blue, reflectivity $R(\theta)$ from the target's surface where the longest ray is at the specular direction; and in green, reflectance from the target's volume (scattering within the volume and transmission through it.

Detection models are based on constructing a test statistic derived from the probability density function (*pdf*) of the data (e.g., BRDF measurements). The objective is to choose between two hypotheses regarding the measured data: H_0 and H_1. The null hypothesis, H_0, is that the data does not contain the target-signal of interest (i.e., there is no chemical contamination on the surface, hence, H_0 is "background" data), and H_1 is the alternative hypothesis that the data contain the target-signal of interest. Usually it is assumed that auxiliary H_0 data are available from previous measurements and can be used to aid the detection decision. We show that in this study that reliable "clean" background measurements may not be available (due to non-uniformity of the surface) and detection may have to rely only on H_1 data. The detection problem is simply stated as a binary Neyman-Pearson decision problem[7]: given measurement M, should the measurements be labeled as belonging to class H_0 or to H_1. Formulation of the model to explain the measurements M is a first important step for solving the detection problem; and is the main thrust of this work.

Our objective in this work is to produce a model that sufficiently explains the three bundles of energy in Figure 1. That is, given spectral measurements M and a known target absorption spectrum α (e.g., obtained from a reference database) we seek a mathematical transformation $M = \xi(\eta|\alpha)$ (reads ξ as a function of η for a given α) and solve for the parameter set η. The transformation function ξ is the model, and mathematically such a transformation always exists. Our goal is to find a *meaningful* model, i.e., a physically based transformation function ξ that by being physical it may: (a) capture a smaller size of the many possible functions, (b) lend confidence that it is a plausible (i.e., "correct") model—especially when it produces a physical parameter set η, and (c) exhibit specificity to correct input α, that is, given

3

the wrong absorption spectrum as input, the model should fail to fit the data. Ideally, the model should also be simple enough so that the optimal parameter set is easily found via numerical optimization methods. In our radiative transfer model the equations rely nonlinearly on the parameters, and we are not always successful at producing a physical parameter set. Nevertheless, a non-physical parameter set does not necessarily invalidate the physical model, but may suggest that the model is too simple or that there exists some mathematical non-uniqueness in the solution.

Scattering theories for rough surfaces and deposited targets do exist (e.g., see references 4-6) but are extremely complicated and in most cases the input required for implementing the theory (e.g., statistical characterization of the roughness) are extremely difficult to obtain in practice. As an example of the complexity of the contaminated surfaces considered in this work, micrographs of potassium chlorate deposited at 50 µg/cm^2 on rough aluminum are shown in Figure 2. The contamination is irregular in shape, neither uniform nor homogeneous. Figure 2 immediately puts in question the feasibility to mathematically characterize the morphology of the contamination. Furthermore, we wish to keep the model as general as possible so that it may be applicable to contaminated surfaces with different deposition characteristics or surfaces with different roughness and spectral behavior. Thus, in this study we strive to use an empirical approach (e.g., fitting the measurements with empirical equations) in conjunction with basic theoretical principles that leverage scattering theories. Hence, our objective is to develop a theory that can be used in practical applications and strikes a balance between complexity (derived from theory) and simplicity (derived from empirical approach or from the use of simplifying assumptions applied to the theory).
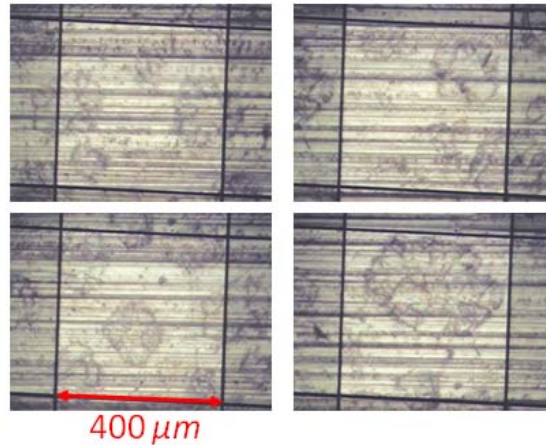
Figure 2. Rough aluminum surface (long horizontal grooves are visible) with potassium chlorate deposits (50 µg/cm^2). The irregularities of the contamination are clearly seen. The fill factor *f* is the fraction the area occupied by target and is ~0.4.

In our model we ignore multiple reflections (i.e., nonlinear interactions) between the target and the bare substrate, and so the basic model equation is a linear combination target and background (bare substrate) radiances given by:

$$M = (1-f)M_0 + f M_1 \qquad\qquad (1)$$

where f is the fill-factor of the contaminated surface (i.e., the fraction of the surface area that is contaminated), M_0 is the portion of the measured signal due to the background (red rays in Figure 1) and M_1 is the portion of the measured signal due to the contamination (blue + green). The reflectance of the contaminated surface (illuminated with incident radiance L) is given by:

$$R = \frac{M}{L} = (1-f)R_0 + f\,R_1 \qquad\qquad (2)$$

Where $R_0 = M_0/L$ is the reflectance of the bare substrate and $R_1 = M_1/L$ is the reflectance of the contaminated region (target). Due to the aforementioned complexity of modeling scattering phenomena, the scattering contribution of the target-volume effect is ignored in our model with only the two-way attenuation contribution (due to absorption) of the volume term explicitly modeled. Therefore, the attenuation coefficient due to absorption, α, is an important input for the model.

The remainder of this report is organized as follows. Section 2 presents key scientific issues that impacted the development of the model. Section 3 presents the reflectance model for contaminated rough surfaces, and results of applying the model to laboratory data. Section 4 presents theory and results of a radiative transfer model for field data. Section 5 is a summary, which includes a list of key innovations and insights, unanswered questions, and future research topics. Specific recommendations are called out in Section 6.

2.   KEY ISSUES

The key issues that we are concerned with are:

- Reflectance (BRDF) of a surface
    - Is it Lambertian? How non-Lambertian is it?
    - What is the difference in magnitude between the specular and the diffuse reflectance components?
    - Effect of roughness on surface reflectivity—can we approximate it with a simple model?
- Optical constants for the target as deposited on a surface (effect of morphology) and as measured in transmission with a pellet (i.e., the target is "squeezed" to form a uniform layer)
- Fill factor: Can we estimate it?
- Penetration depth (computed from optical constants)
- How reproducible is the measured surface reflectivity? Does the non-uniformity introduce much variation for the reflectance?

In Section 2.1 we present theoretical aspects of these issues, and the significance to the development of the model. In Section 2.2 we present results of laboratory measurements that support some of the theoretical questions raised in Section 2.1. We employ two instruments for exploring these main issues: (a) A spectrometer with integrating sphere (integrating over all reflectance angles, hence it is not a directional BRDF reflectance) in which we can measure either the transmission of the target material that is finely ground and formed into a pellet with an inert transparent material (spectra are independent of target morphology) or the reflectance of the deposited target on a surface (i.e., with the effect of the deposition characteristics and morphology). (b) An ellipsometer with which we measure the directional reflectance $R(\theta\,|\,\theta_i)$ of a

target deposited on a surface. We can control (within some limitations) the incidence and reflectance angles of the ellipsometer. We view the ellipsometer reflectance lab measurements as closely related to expected reflectance in field data, with the exception that in field data the target is illuminated simultaneously from all incident angles by the downwelling atmospheric radiation that comes from all directions (with unequal intensity) and in the ellipsometer the incidence only comes from one direction.

2.1 THEORY

2.1.1 *BRDF*

At the beginning of this study, we considered whether or not the rough surface is Lambertian. The hope was that if it is Lambertian, then one can simply infer the BRDF from measurements of the surface total reflectivity with an integrating sphere spectrometer (R_{IS}), where the integrating sphere measurements are given by:

$$R_{IS}(\lambda) = \int_{\phi=0}^{2\pi} \int_{\theta=0}^{\pi/2} BRDF(\theta,\phi\,|\,\lambda)\cos(\theta)\sin(\theta)d\theta d\phi.$$ If the surface is Lambertian, then the BRDF is

angular independent and not a function of the spherical angles *(θ,φ)*, and the BRDF is given by *BRDF(λ) = R_{IS}(λ)/π*. Note, that since R_{IS} integrates over all reflectance angles, it is not possible to retrieve the angular dependence of *BRDF(θ,φ | λ)* from a single value of *R_{IS}(λ)* if the rough surface is not Lambertian. It was also noted by Kavaya et al.[8] that "It is tempting to assume that each target's *θ* dependence curve [Kavaya's target is our rough surface] could be scaled absolutely by using the integrating sphere data and the area under the *θ* dependence curve. However, this is not possible for surfaces with general BRDF". For a given incidence direction (say *θ_i*), the *measured* reflectance from a Lambertian surface is *BRDF (θ) ∞ cos (θ)* (i.e., proportional to the cosine of the reflectance angle; see reference 8 for Equation 6, Figure 1a geometry). In Section 2.2.1, we compare our BRDF measurements of diffuse gold and rough aluminum to the expected Lambertian behavior and show that these two surfaces are far from being Lambertian. A brief search in the literature shows[9] that even a diffuse gold surface (manufactured by Labsphere, North Sutton, NH) was measured to deviate quite a lot from the expected ideal Lambertian behavior. The concept of Lambertian surface, while being useful in theoretical derivations, is an ideal concept that rarely occurs.

2.1.2 *REFLECTANCE OF A ROUGH SURFACE (DECAY MODEL)*

We now address the more realistic issue of reflectance (BRDF) for a real rough surface. Siegel & Howell[10] (Ch.5-4.4, p154) notes that as the optical roughness, *σ/λ* (the ratio of the physical roughness standard deviation to wavelength), increases beyond 1, multiple reflections occur in the material cavities, hence, the absorption increases and emissivity (by Kirchhoff's law) increases as well. When *σ/λ < 1* multiple reflections are reduced and the surface behaves more like a smooth surface. However, even for *σ/λ < 1* directional properties of the material (and especially the BRDF) *are* significantly affected by the small roughness. Predicting the effect of roughness on radiative properties of material (e.g., emissivity) is very difficult, in part due to the difficulties in defining the statistical properties and the definition of a "rough surface". The roughness can be defined by root mean squared (*rms*) value of heights, *rms* slopes, distribution function of the size of roughness, horizontal scale of roughness, autocorrelation functions, etc. Therefore, we take a different approach.

To describe the reflectance of a rough surface we resort to a semi empirical method which we based on a theoretical model derived by Baylard et al.[11] We empirically extend their

derivation for a better fit to our observations. The theory predicts that the reflectance is given qualitatively as $\rho(n,k \mid \theta_i)$ x $\exp(-a\lambda^{-2})$ where $\rho(n,k \mid \theta_i)$ is the Fresnel reflectivity (see reference 12 for Equation 43, p45) for un-polarized radiance at incidence angle θ_i, n and k are the refractive index (real and imaginary parts) of the intrinsic surface material (e.g., aluminum refractive index, see Rakic[13]) and a in the exponential decay function $\exp(a\lambda^{-2})$ is a constant that is a function of surface roughness and incidence angle. The quadratic expression $a\lambda^{-2}$ is related to the optical *rms* roughness of the surface. We found this expression to fit the data poorly with regard to wavelength dependence of measured reflectance of rough aluminum. The results of Baylard's theoretical model were focused more on explaining the angular dependence of the reflectance at a single wavelength rather than the wavelength dependence of the reflectance at a particular angle. In our study, where identification and detection of the target material is done based on spectral response, we are interested in the wavelength dependence response of the reflectance at a given geometry (i.e., at a set incidence and reflected angles).

To improve the fit to measured rough surface reflectance data we extended the decay function to be more general (using a second order polynomial in wavenumber λ^{-1}) in the form of $D(a,b,c \mid \lambda) = \exp(a\lambda^{-2} + a\lambda^{-2} + c)$, where the coefficients (a,b,c) are determined by a fitting procedure of observed (measured) reflectance data from a rough surface. We did not want to deviate too much from Baylard and thus did not add higher order terms (e.g., λ^{-3} and λ^{-4}). Our reflectance model for a rough surface is given by

$$\left\{ \begin{aligned} &R(\theta \mid n,k,\theta_i,\lambda) = \rho(n,k \mid \theta_i) \times D(a,b,c \mid \lambda) \\ &D(a,b,c \mid \lambda) = \exp(a\lambda^{-2} + b\lambda^{-1} + c) \\ &(a,b,c) = \arg\min_{a,b,c} \left\| data(\theta) - R(\theta) \right\|^2 \end{aligned} \right\} \qquad (3)$$

Where $\| \ \|$ denotes the Euclidean vector norm. Thus, the coefficients are implicitly a function of θ and θ_i. In principle we can obtain the BRDF of the surface if we have $data(\theta)$ for all angles θ and for all incidence angles θ_i and then we derive with Equation 3 the roughness coefficients (a,b,c) for all angles; hence $R(\theta) \rightarrow BRDF\ (\theta,\theta_i)$. This highlights a disadvantage to the semi-empirical approach in that the physical meaning of the decay coefficients is lost, and the decay model loses the ability to be predictive. It may be possible with controlled experiments to derive an empirical dependence of the coefficients (a,b,c) on θ, θ_i, and the roughness characteristics of the surface.

The behavior of the exponentially decay function can be explained qualitatively as follows. For a perfectly smooth surface the reflectance at the specular angle is given by the Fresnel reflectance, $\rho(\theta_i)$, and there is no diffuse reflection (i.e., reflectance is zero at $\theta \neq \theta_i$). As the surface roughness increases, the optical roughness does also, but does so proportionately to λ^{-1} (wavenumber). As the surface appears rougher with respect to the incident wavelength, more energy is transferred from the specular direction to other directions. Thus, at the specular angle the reflectance of a rough surface should exhibit a loss compared to a smooth surface; the loss is greater for shorter wavelengths, and we expect that the decay function should decrease as a function of wavenumber. For off-specular (diffuse) angles, there is a gain due to the transference of energy from the specular angle; the gain should be greater at shorter wavelengths (due to greater optical roughness), and the decay function should increase with increasing wavenumber. The quadratic exponential decay function can both increase and decrease with wavenumber and therefore mathematically is a good candidate for both specular and off-specular angles. Because the effect of roughness is viewed as either a loss or a gain

from the reflectance of a smooth surface, we expect $R(\theta) \leq \rho(\theta_i)$ and the decay function to satisfy $0 \leq D < 1$. Note that for a smooth surface, $(a,b,c) \to 0$, $D(a,b,c \mid \lambda) \to 1$, and $R(\theta) \to \rho(\theta_i)$. In Figure 3 we show schematically the behavior of reflectance model for a rough surface. The difference between the Fresnel reflectance ρ and $R(\theta) = \rho \times D(a,b,c)$ is the energy that is transferred from the specular reflectance direction (coherent scattering) into other angles (diffuse scattering). As wavelength decreases and optical roughness increases, more energy is transferred.
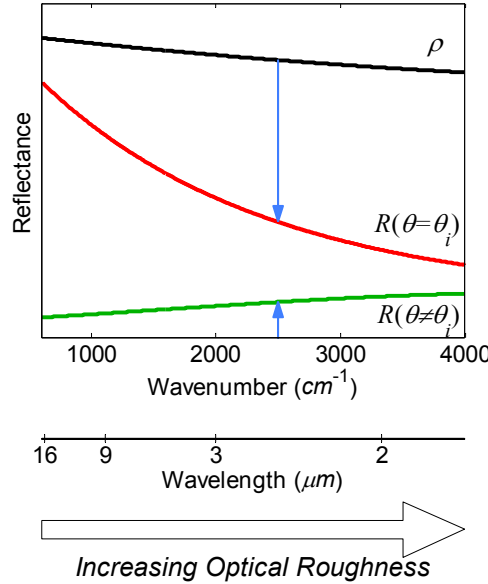
Figure 3. Behavior of reflectance model for a rough surface. In black: the reflectance of a smooth surface (Fresnel reflectance). In red, the reflectance at specular angle $\theta = \theta_i$; in green, the reflectance at off-specular angle $\theta \neq \theta_i$.

It is interesting to note that wavelength dependence (at three laser wavelengths: 0.63, 3.39 and 10.6 µm) for backscatter reflectance from rough metallic surfaces (ratio of *rms* roughness height to wavelength > ¼) was studied experimentally as a function of the incidence angle by Cheo and Renau[14]. The total backscattered wavelength dependence was found to be of the form λ^q where *-0.8 < q < -0.4* as a function of incidence angle (20° to 80°). For near normal incidence the backscatter reflectance was found to be independent of wavelength (i.e., $q \approx 0$). In the radar literature Katz[15] showed that the reflectance (i.e., the radar cross-section) of land and sea surfaces (the surfaces can be viewed as rough surfaces at radar frequencies), on the average, follow approximately a λ^{-1} behavior (although the exponent q in may vary from +2 to −6 in individual cases). From theoretical considerations[16] radar reflectance would vary inversely with transmitted wavelength (as λ^q, $q < 0$) . Radar reflectivity of sea breezes (reference 17, p261) exhibited exponents in the range +2 to –4. These observations of wavelength dependency (although our wavelength region is far from radar wavelengths) encourage us that the more general form of the decay function we adopted empirically may have a stronger underlying basis. Note that for small values of (a,b,c) the decay function

$D(a,b,c \mid \lambda) \xrightarrow{(a,b,c) \to 0} 1 + a\lambda^{-2} + b\lambda^{-1} + c$ which can express the spectral dependence of rough surfaces as observed in radar. More generally, the power series expansion of the exponential function can be used to show that our decay function has a dependence on all powers λ^q, $q \leq 0$.

Multiplicative property of the decay function: Due to the exponential form of the decay function, Equation 3, a rough surface that "becomes" rougher (e.g., due to applying more

machining processes) can be presented as $R(\theta) = \rho \times D(a,b,c) = \rho \times D(a_1,b_1,c_1) \times D(a_1,b_1,c_1) = \rho \times D(a_1 + a_3, b_1 + b_2, c_1 + c_2)$, where (a_1,b_1,c_1) are roughness parameters due to roughness of the initial surface, (a_2,b_2,c_2) is the increased roughness parameters that produced the final stage roughness $D(a,b,c)$, and the roughness parameters of the final stage are $(a,b,c) = (a_1 + a_3, b_1 + b_2, c_1 + c_2)$. It is also interesting to note that mathematically we can reverse the roughness process (i.e., we can smooth the rough surface) to obtain $\rho = R \times D(-a,-b,-c)$. We remind the reader that we do not currently know how to predict the roughness parameters (a,b,c) form physical roughness parameters of the rough surface.

Significance: Modeling the reflectance of a rough surface is the first step towards building a model for a *contaminated* rough surface. In Section 3.2.5 and 4.2.2 we will show that auxiliary H_0 measurements can be substituted for the theoretical Fresnel reflection, and used successfully in the radiative transfer model in the case that n and k of the substrate is unknown.

2.1.3 *OPTICAL CONSTANTS (N,K) AND TARGET'S ABSORPTION COEFFICIENT A*

The target material is characterized by its complex spectral refractive index $n + ik$. The refractive index is an intrinsic property of the material regardless of the morphology (e.g., the shape of the target deposits on the surface). The optical constants for the deposited target are of general interest for building library of targets and also important as an input to our radiative transfer model via the function $g\Delta n$ (discussed in Section 3); α, the absorption coefficient, is also an important input to our radiative transfer model. The optical properties of the target (e.g., absorption, scattering, and extinction coefficients) are all complicated functions of the morphology of the target (shape, orientation, etc.) as well as of the intrinsic refractive indices.

Given a target material we can measure its extinction coefficient, α_{ext} (extinction is the sum of absorption and scattering), via transmission measurements $t(h)$ for a known pathlength h: $t(h) = \exp(-\alpha_{ext}h)$. The typical procedure is to finely grind the target material of mass m in grams, dilute it in a potassium bromide (KBr) mixture to create a pellet with cross-section A (cm^2) and perform transmission measurements, where the average pathlength h is calculated from m, A, and the specific density d (g/cm^3) of the material (where $h = m/(d \cdot A)$). However, by placing the pellet in the entrance port of the integrating sphere – which detects all forward-scattered photons – the transmission losses due to scattering are reduced (idea credit to Barry Williams). We assume that losses due to scattering into the backward hemisphere (i.e., outside of the integrating sphere) are negligible, and that the resulting extinction coefficient is due to absorption only. Therefore, $\alpha_{pellet} = - ln(t)/h$ is a good estimate of the intrinsic absorption coefficient of the material. The imaginary part of the complex refractive index can be obtained from the absorption coefficient via Equation 6 (below) and the real part may be obtained via Kramers-Kronig (KK) analysis,[18] $n = KK(k)$, discussed further below. If α_{pellet} is an accurate measure of the absorption coefficient of the material, then the derived (n, k) will be good estimates of the intrinsic refractive index of the material.

In our study, the material of interest is deposited non-uniformly with some morphology onto a rough surface. The morphology of the deposited target depends on the deposition technique, the material physical properties (such as viscosity, temperature, etc.), and the physical properties of the surface (e.g., surface tension). This will affect the optical properties of the material, including its absorption coefficient. Given knowledge of the morphology and the intrinsic (n, k) indices in principle would allow computation of absorption (and extinction) coefficients of the deposited material. However, due to lack of knowledge and the complexity of such a computation, we wish instead to *measure* the absorption coefficient of the deposited

material to obtain a more appropriate estimate of the absorptivity than is given by the KBr pellet method (which is largely morphology-free).

Our approach for obtaining α from a contaminated surface is as follows. Reflectance measurements, R, of the contaminated rough surface are made in the integrating sphere. Because the integrating sphere captures all scattered photons, the losses are due only to the reflectivity of the substrate, the reflectivity of the target, and the two-way attenuation (by absorption) from the volume of the deposited material. We assume that the reflectivity of the target is negligible and therefore only red and (a portion of) green rays in Figure 1 contribute to the measurements. Under these conditions, (2) can be written as

$$R = (1 - f)R_0 + fR_0 e^{-2\alpha h} = R_0(1 - f + fe^{-2\alpha h}) \tag{4}$$

where $e^{-2\alpha h}$ is the two-way attenuation dependent upon the average pathlength h through the material, R_0 is the reflectance of the bare substrate, and f is the fill factor. Although it may be possible to determine f and R_0 from auxiliary measurements, in practice f, R_0, and h are not known. Since neither h nor α is known, the best one can hope for is to solve for the combined unknown αh. This is an ill-posed problem, and additional constraints or assumptions must be imposed to make the problem tractable.

The first simplifying assumption is that the optical depth of the material is small ($2\alpha h \ll 1$) so that the exponential may be linearized, obtaining $R \cong R_0 (1 - 2\alpha h f)$. Since $f \leq 1$, it must be that $2\alpha h \ll 1$ and, therefore, $R \cong R_0 e^{-2\alpha h f}$, which can be verified with a first-order Taylor expansion of the exponential. Physically, this simplification says that if the optical depth is small, there exists an equivalent film with a fill factor of 1 and a reduced thickness equal to hf.

The second assumption is that the substrate reflectance, R_0, may be estimated from a baseline fit, B, to the negative logarithm of the reflectance. Taking the negative log of $R \cong R_0 e^{-2\alpha h f}$ one obtains $-ln(R) \cong -ln(R_0) + 2\alpha h f$.

We assume that the smooth baseline regions around absorption peaks correspond to regions where α is small, and that a baseline fit derived from these regions approximates the $-ln(R_0)$ term. Fitting a baseline is subjective, and requires identification of spectral bands that lack absorption features to use in the fitting (we identify spectral bands that lack absorption features via inspection, guided by previous measurements of α_{pellet}). It also requires assuming a functional form for the baseline. We are guided by the decay model (Section 2.1.2) and use a quadratic polynomial with respect to wavenumber to fit the baseline, B; the goal is for $B = -ln(R_0)$. Note that if the Fresnel reflectance of the bare substrate, ρ_0, is known, then $-ln(R) = -ln(\rho_0) - ln(D) + 2\alpha h f$ can be rearranged to read $-ln(R) + ln(\rho_0) = -ln(D) + 2\alpha h f$, where the left-hand side is known. A baseline fit with a quadratic polynomial performed on $-ln(R) + ln(\rho_0)$ is then an approximation of the decay function. Also, note that a baseline by its very definition is smooth; sharp spectral features present in the substrate reflectance will likely be attributed to absorbance from the target. Conversely, it is possible that smooth or very broad absorption effects are erroneously captured in the baseline and, therefore, it will only be approximately true that $B \cong -ln(R_0)$. The baseline-subtracted measurements $-ln(R) - B \cong 2\alpha h f$ may be solved for the combined term $\alpha h f$. This quantity has the correct spectral shape, but it is not in the correct units of cm^{-1}. To determine an estimate of hf and, therefore, obtain a quantitative α in cm^{-1}, we identify a similar spectral feature common to both α_{pellet} and $\alpha h f$. We assume that for this spectral feature $\alpha(\{1/\lambda_0\}) = \alpha_{pellet}(\{1/\lambda_0\})$, where we use the notation $\{1/\lambda_0\}$ to denote all the wavenumbers that are within the common feature. The solution for the unknown product hf is given by,

$$hf = E_{\{1/\lambda_0\}}\left[\frac{-\ln R - B}{2\alpha_{pellet}}\right] \qquad (5)$$

where $E_{\{1/\lambda_0\}}[\cdot]$ is the expectation operator (mean) taken over the set of wavenumbers $\{1/\lambda_0\}$, or can be solved as a least-squares problem; note that more than one spectral feature may be used. The final solution for α is given by $\alpha = (-\ln(R)-B)/(2hf)$, where hf is given by Equation 5.

With α in the units of cm^{-1}, we can obtain k (Equation 6, below) and $n = KK(k)$. We view the refractive index n as an "effective refractive index" in the sense that it "captures" the effect of the morphology of the target and thus may be better suited for modeling the specific scenario (using the $g\Delta n$ term that is introduced in Section 3.1.1). If we cannot find a specific common feature to calibrate α, then other choices are possible, for example, by requiring the vector norm of α and α_{pellet} to be identical. Error in this calibration procedure will cause the estimate of α to have the wrong magnitude; if the magnitude is overestimated, resulting estimates of the mean target height, h, inferred from α will be underestimated. If the magnitude of α is underestimated, the inferred value of h will be too large. Even if some error is suspected in the calibration procedure, we feel that the calibration procedure is still justified, in that it will at least produce values with the proper order of magnitude. Further, for detection and identification purposes, having the correct spectral shape is more important than having the correct magnitude, and a poor calibration will still preserve some important spectral features of the target material and its morphology. Results of the calibration procedure applied to potassium chlorate on rough aluminum (and of a slightly modified procedure applied to ammonium nitrate) are presented in the results Section 2.2.3.

Significance: If α_{pellet} is close enough in spectral shape to the observed spectrum from the deposited material, then it may be successful in modeling the reflectance from contaminated rough surfaces. The advantage of this is that a single measurement of α_{pellet} per material of interest might then be sufficient to populate a reference database. On the other hand, if the effects of the deposition morphology are strong, α may be needed for more accurate modeling of the observed reflectance. Since there may be many different morphologies, this approach would require an expanded reference library with more than one reference spectrum per material.

Kramers-Kronig Relations: The Kramers-Kronig relationship is a statement of causality between the real and imaginary parts of the complex index of refraction, $n + ik$. For homogeneous medium (without internal scattering) the imaginary part of the refractive index is given by (see reference 18, Equation 2.52) as

$$k = \frac{\lambda\alpha}{4\pi} \qquad (6)$$

where α (cm^{-1}) is the absorption coefficient (i.e., no losses due to scattering) and λ is wavelength (cm). The real part of the refractive index is given by

$$n(\lambda) - n_\infty = 2\pi^{-1}\int_0^\infty \frac{\lambda'k(\lambda')}{\lambda'^2 - \lambda^2}d\lambda'$$

$$= 2\pi^{-1}\int_0^{\min\lambda} \frac{\lambda'k(\lambda')}{\lambda'^2 - \lambda^2}d\lambda' + 2\pi^{-1}\int_{\min\lambda}^{\max\lambda} \frac{\lambda'k(\lambda')}{\lambda'^2 - \lambda^2}d\lambda' + 2\pi^{-1}\int_{\max\lambda}^\infty \frac{\lambda'k(\lambda')}{\lambda'^2 - \lambda^2}d\lambda'$$

$$= \Delta n + e \qquad (7)$$

where $n_\infty = 1$, $\min \lambda$ and $\max \lambda$ denote the minimum and maximum wavelengths available in the data (the measured spectrum k; in this study that range is ~500 cm^{-1} to ~4000cm^{-1}),

$\Delta n = 2\pi^{-1} \int_{\min \lambda}^{\max \lambda} \lambda' k(\lambda') d\lambda' / (\lambda'^2 - \lambda^2)$ (the second term from the second line of Equation 7 is

directly computable from the data, and e is a scalar constant that is the energy that may not be directly computed due to lack of data (the first and third terms from the second line of Equation 7. However, e may be estimated, for example, by knowing the value of the refractive index, $n(\lambda_0)$, at a reference wavelength (e.g., for potassium chlorate the refractive index is 1.408035 at $1/\lambda_0$ = 16969.3 cm^{-1}, which is the sodium D line), we can write Equation 7 as $n(\lambda_0) = \Delta n + n_\infty + e$ and

solve for e. Knowing e, $n(\lambda)$ may be computed for any wavelength between $\min \lambda$ and $\max \lambda$.

We note that for irregular non-uniform and inhomogeneous material (see potassium chlorate target on aluminum in Figure 2 using Kramers-Kronig relationship with Equation 6 is problematic, but we do not have an alternative, and when we measure spectral transmission with an integrating sphere spectrometer (from which α is deduced), we do indeed measure only absorption losses (the integrating sphere collects all scattered energy). Thus, using Equation 6 is somewhat justified in the sense that it is some "effective α" for the material. Note that if k is multiplied by a constant, the resulting n will also be multiplied by that constant.

2.1.4 *FILL FACTOR (F) AND AVERAGE THICKNESS (H)*

When the target is visible in the image (e.g., Figure 2) imaging processing tools such as morphological operators (opening, closing, dilation and erosion) can be used to enhance the image and to compute the fill factor (fraction of area covered by the target).

Knowing the density d (g/cm^3) of the target, the deposit surface concentration d_S (g/cm^2) of the surface, and the fill factor f, we can estimate an average thickness (in cm) as $h=d_S/(fd)$. This average thickness (as a rough estimate) can be compared to penetration depth and give us an indication to the importance of incident photons completely penetrating the target. From known characteristics of the deposition process, it is expected that the average thicknesses of our samples will be less than a few microns.

2.1.5 *PENETRATION DEPTH*

The issue of penetration depth is connected to the relative importance of the two-way attenuation contribution compared to the scattering contribution in the target volume term (green rays in Figure 1). The penetration depth z at which transmission of radiation traveling perpendicularly through a layer of thickness *h* reaches $1/e \cong 0.37$ is simply given by the reciprocal of the absorption coefficient of the material (Ref 19, p268), i.e., for a homogeneous medium

$$z = \frac{1}{\alpha} = \frac{\lambda}{4\pi k} \tag{8}$$

Due to conservation of energy, whatever portion of radiation that is not transmitted has the potential to be either scattered or absorbed; comparing penetration depth (which relates to absorption) to the expected thickness of the material establishes whether the scattering portion is expected to be significant. If the penetration depth is very small, then two-way attenuation term will be small, meaning that the term we ignore in the radiative transfer model (the scattering portion of the volume effect in Figure 1) is more likely to be important.

Note that if a perfectly reflective surface is located at the penetration depth, the total fraction of radiation leaving the layer due to two-way attenuation is ~10%.

Significance: if $z >> h$ where h is the thickness of the deposited target material, then nearly all of the incident radiation will interact with the substrate and one can expect (for a highly reflective substrate) that much of the measured signal from the contaminated surface will be due to two-way transmission (in and out of the material).

2.1.6 *UNIFORMITY OF ROUGH SURFACES*

We do not think that one can expect that the underlying surface will be uniform and can be sampled from another independent location (H_0 scenario), and be applicable without modification to the H_1 scenario. The aluminum substrate that was used in this study is neither isotopic in its roughness features (e.g., there are long grooves etched in the Home Depot material) nor it is it homogeneous.

Significance: If H_0 cannot be obtained reliably, detection decisions must either on H_1 measurements only, or there must be a mechanism to allow for the H_0 measurements to be modified so that the inherent variability has less impact. We will demonstrate in Section 3.2.5 and 4.2.2 that the decay model can allow the use of auxiliary H_0 measurements.

2.2 RESULTS

2.2.1 *BRDF FOR GOLD AND ALUMINUM*

Our objective is to evaluate how Lambertian or specular (see Section 2.1.1 for definitions) the reflectivity of a surface is. If the surface is Lambertian then its BRDF is not angularly dependent, and it can be easily deduced from reflectance measured with the integrating sphere. If the BRDF is highly directional (close to specular), then it greatly simplifies the radiative transfer model (Equations 9, 10, and later Equation 11) where most of the information on the target's presence would be determined by two-way transmission of the incidence radiation measured at the specular reflectance angle. From the ellipsometer directional reflectance measurement $R(\theta)$ where θ is measured in the specular plane (the plane spanned by the incidence and the specular reflectance, defined as the $\phi = 0$ plane) we reconstructed (for illustrative purposes) the complete *BRDF (θ,ϕ)*. We assumed azimuthal symmetry with regard to *(θ,ϕ)*, i.e., same reflectance for any combinations of *(θ,ϕ)* for which the scattering angle is the same (see reference 20, Equation 3.4.7).

In Figure 4 (left plot) we show the ellipsometer measurements (at $\phi = 0$) for a diffuse gold surface (Pike Technologies, Madison, WI) and the predicted reflectivity of a Lambertian surface as a function of the reflectance angle ($\infty \, cos(\theta)$). The BRDF is an average BRDF for wavelength range 4 to 7μm. The figure clearly shows that the diffuse gold is not Lambertian, nor is it entirely specular. Note that the peak is slightly shifted from the specular position (60°), this slight shift is not due to measurement error but can be explained theoretically[21] based on the geometry of mirror-like facets that are used to model the rough surface. In the right plot of Figure 4, the 3D reconstruction is shown. The Lambertian prediction is shown as a sphere (the distance between the gold surface and the envelope of the sphere follows a cosine dependence). The reconstructed BRDF clearly deviates from being Lambertian, even for a specially made diffuse gold surface. Hence, we do not think that other rough surfaces will be found to be Lambertian, and the integrating sphere is unlikely to be able to directly provide an estimate of the BRDF.
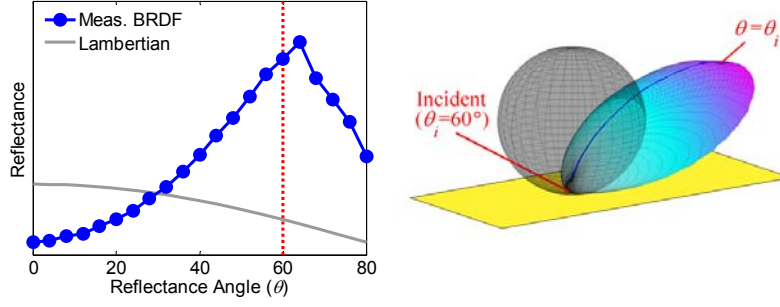
Figure 4. BRDF for a diffuse gold surface measured (Pike Technologies, Madison, WI). *Left*: **measured reflectance (blue dots) in the specular plane as a function of reflectance angle and predicted Lambertian reflectance (in solid grey).** *Right:* **reconstructed 3D BRDF (ellipsoidal shape) with predicted Lambertian response (gray sphere).**
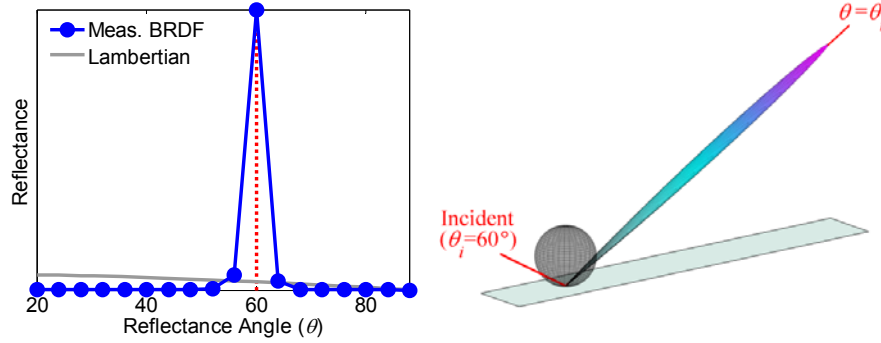
Figure 5. BRDF for Home Depot rough aluminum surface. *Left*: **measured reflectance (blue dots) in the specular plane as a function of reflectance angle and predicted Lambertian reflectance (in solid grey).** *Right:* **reconstructed 3D BRDF.**

In Figure 5 we show the measured and reconstructed BRDF of the rough aluminum. The figure shows that the measured BRDF is vastly different than that of a Lambertian surface, with an intense specular peak (~×20 more intense relative to off-specular directions). The figure shows that most of the angular reflectance occurs within a narrow cone (~±5°) around the specular direction (60°).

2.2.2 *ANGULAR REFLECTANCE FOR ROUGH ALUMINUM (DECAY MODEL)*

We used our rough surface reflectance model (Equation 3) to fit the angular reflectance measurements of bare aluminum (measured with ellipsometer). The Fresnel reflectance ρ_0 at incidence angle of 60° for aluminum was computed with refractive indices taken from Rakic[13]. In Figure 6 we show the ellipsometer rough surface reflectance measurements at various incident and reflectance angles. The left plot shows specular reflection and two off-specular angles (56° and 64°) for 60° incidence. The right plot shows results at incident angle 32° and two off-specular angles. Model results (dotted black curves) fit the data well: in all cases the residual is less than ± 0.02 reflectance units.

14
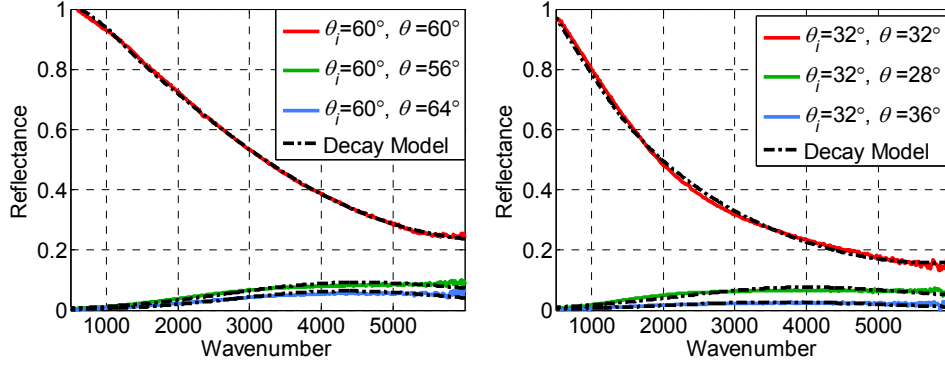
Figure 6. Results of fitting the decay model to angular reflectance for rough aluminum.

The roughness coefficients *(a,b,c)* for the model when applied to 60° incidence are $(-1.50 \cdot 10^{-8}, 7.71 \cdot 10^{-5}, 0.0665)$ for the specular direction, and $(-1.76 \cdot 10^{-7}, 1.83 \cdot 10^{-3}, -5.86)$ and $(-2.29 \cdot 10^{-7}, 2.25 \cdot 10^{-3}, -7.02)$ for the off-specular directions of 56° and 64°, respectively. For 32° incidence, the roughness coefficients are $(4.21 \cdot 10^{-8}, -3.11 \cdot 10^{-4}, 0.190)$, $(-1.45 \cdot 10^{-7}, -1.53 \cdot 10^{-3}, -5.26)$, and $(-1.83 \cdot 10^{-7}, 1.69 \cdot 10^{-3}, -6.37)$ for reflectance angles 32°, 28°, and 36°, respectively.

2.2.3 *ABSORPTION COEFFICIENTS FROM ROUGH CONTAMINATED SURFACES*

Measurements of potassium chlorate and ammonium nitrate at 50 µg/cm^2 deposited on rough aluminum were made in the integrating sphere. Figure 7 shows results of the calibration procedure for potassium chlorate, and compares the resulting α and α_{pellet}. An absorption feature at 1900 cm^{-1} with identical shape in the reflectance measurements and in the KBr pellet measurements was used to calibrate the absorption spectrum, according to the procedure in Section 2.1.3. Overall, the spectral shape of α and α_{pellet} for potassium chlorate is similar, however, for the strongest feature (which occurs in the LWIR region at around 970 cm^{-1}) there are some clear shape differences. Whereas α_{pellet} shows one major peak (with a small secondary feature at 940 cm^{-1}), α shows a clear doublet (peaks at 935 and 995 cm^{-1}). This difference in spectral shape may be explained by the combined effects of anomalous dispersion and surface roughness, which can cause a single absorption peak to appear as a doublet when measured in reflectance (see reference 5, Ch. 11, p306). The insets in the bottom of Figure 7 shows spectral response from 800-1200 cm^{-1}, which is the LWIR region where there is a major absorption feature for potassium chlorate, and the common feature used for calibration at 1900 *cm^{-1}*.
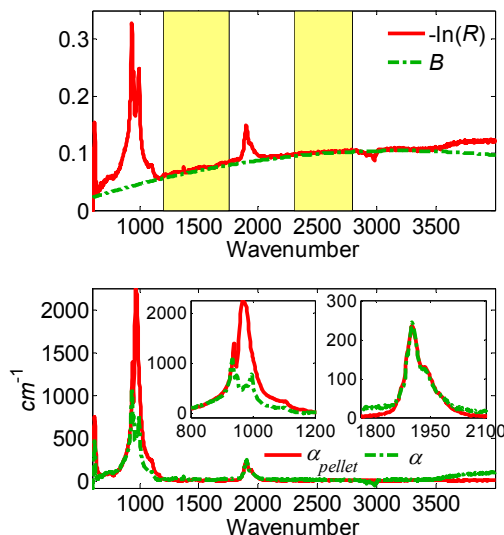
Figure 7. *Top*: **Integrating sphere measurements of reflectance for potassium chlorate deposited on rough aluminum shown in log-space (red); baseline wavenumber-regions (yellow) and baseline estimate (green dotted curve) also shown.** *Bottom*: α_{pellet} **and the calibrated** α **are plotted in red, and green, respectively.**

Figure 8 shows the results of calibrating an ammonium nitrate reflectance spectrum. The procedure in Section 2.1.3 was slightly modified due to a baseline present in α_{pellet}. Prior to calibration, a baseline fit to the pellet absorption spectrum, B_{pellet}, was found. Calibration was then performed with respect to $\alpha_{pellet} - B_{pellet}$ using least squares on the three sharp absorption features present in both pellet and reflectance spectra (from 750 to 1075 cm^{-1}). The pellet baseline was then added back into the solution $\alpha : \alpha \rightarrow \alpha + B_{pellet}$. This modified procedure gave a closer correspondence between the α and α_{pellet} spectra. Overall, the spectral shape between the two is similar, with the most significant differences appearing at 1200-1500 and 2800-3300 cm^{-1}. In the LWIR region the spectra are very similar. The inset in the bottom plot of Figure 8 shows three sharp spectral features (in the LWIR region) that were used for calibration.

16
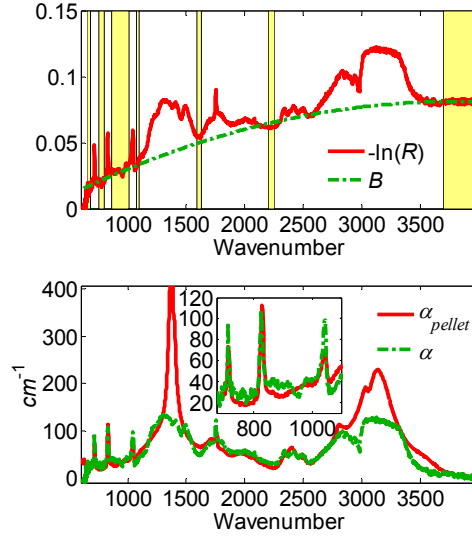
Figure 8. *Top*: **Integrating sphere measurements of reflectance for ammonium nitrate deposited on rough aluminum shown in log-space (red); baseline wavenumber-regions (yellow) and baseline estimate (green dotted curve) also shown.** *Bottom*: α_{pellet} **and the calibrated** α **are plotted in red, and green, respectively.**

The refractive indices of ammonium nitrate measured using the KBr pellet method compare favorably to literature values[22] in terms of spectral shape, however, the magnitude of the imaginary index, k, was about a factor of 80 smaller than the literature value. For potassium chlorate, we observed estimated values of k that were an order-of-magnitude too small (compared to in-house polarimetric ellipsometry measurements). We speculate that in the KBr method, the ammonium nitrate and potassium chlorate particles were not ground finely enough, causing diffraction around the particles. As a result, the incident light in the transmission measurements did not interact with the entire mass of material in the pellet, causing the estimated α_{pellet} (and therefore k) to be too small. This will impact estimates of the penetration depth (Section 2.2.5) and the average thickness of the target material inferred by the radiative transfer model (Sections 3 and 4), causing values that are too large.

2.2.4   *FILL FACTOR AND AVERAGE THICKNESS*

With image analysis techniques we enhanced the contours of the potassium chlorate deposited on rough aluminum. By counting the number of target's image-pixels above a given threshold we deduced that the fill factor for surface concentration of d_S = 50 µg/cm^2 was $f \cong 0.4$. The average thickness is estimated to be on the order of $h = d_s / (fd) \cong 0.5$ µg where the potassium chlorate density is d = 2.34 g/cm^3.

2.2.5   *PENETRATION DEPTH*

The penetration depth (Equation 8) for potassium chlorate and ammonium nitrate are shown in Figure 9. Two curves are shown for each material: penetration depth derived from integrating sphere measurements α_{pellet}; and penetration depth computed after multiplying α_{pellet} by a factor to account for the observed magnitude discrepancies in the measured value of k using the pellet method (see Section 2.2.3). The figure shows that the penetration depth for potassium chlorate is larger than a few microns for the majority of the spectral range. The minimum penetration depth for potassium chlorate is about half a micron near 970 cm^{-1}. From

17

the previous section, the expected thickness of potassium chlorate is also around half a micron. Thus, at the absorption feature near 970 cm^{-1}, it is less likely for the two-way attenuation contribution to dominate the scattering portion of the potassium chlorate volume term (green rays, Figure 1). On the positive side, since a small proportion of radiation reaches the substrate, it is less likely for spectral features associated with the substrate to contaminate the potassium chlorate spectral features at this wavelength range. Penetration depth for ammonium nitrate is qualitatively similar as for potassium chlorate: for most wavelengths, the penetration depth is larger than a micron (1x10^{-4}). The minimum penetration depth occurs at 1500 cm^{-1} at approximately 0.2 µm.
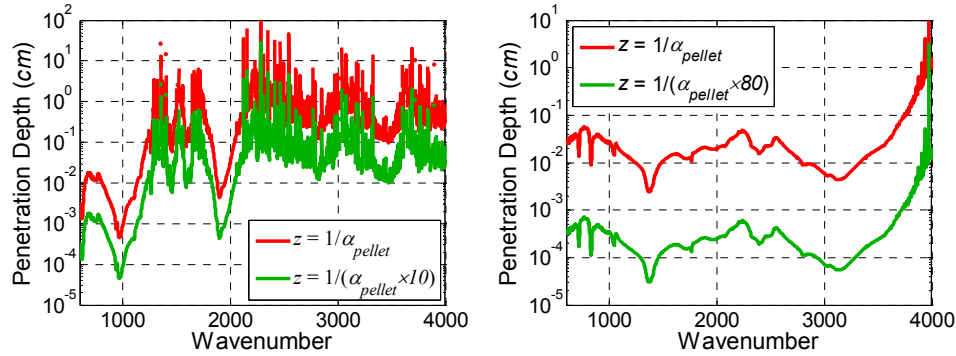
Figure 9. Penetration depth, *z*, of potassium chlorate (left) and ammonium nitrate (right). Two curves are shown in each plot to represent the magnitude discrepancy using the KBr method (see Section 2.2.3).

These results give us the expectation that neglecting the volume scattering term in our radiative transfer model (Sections 3 and 4) should be reasonable for these materials at the concentrations studied.

2.2.6   *UNIFORMITY OF ROUGH ALUMINUM*

Reflectance integrating sphere measurements for the rough aluminum at different orientations and samples of the rough aluminum produced variability of up to 6%) in magnitude. The spectral shape did not change much. The measurements are shown in Figure 10 (left). While these total reflectance measurements exhibit relatively small variations, directional reflectance measurements (measured with ellipsometer) exhibited large variations (tens of percents) and also large differences in spectral shape (see right plot of Figure 10). We therefore caution against assuming that H_0 spectral signature can reliably be transferred from one location to another.
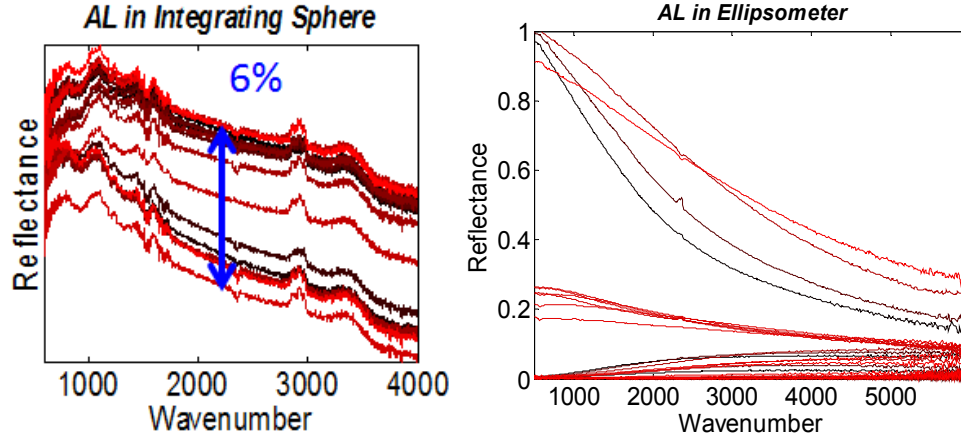
Figure 10. Reflectance due to non-uniformity of rough aluminum. *Left:* **total reflectance measured with integrating sphere.** *Right:* **angular reflectance measured with ellipsometer.**

3.   RADIATIVE TRANSFER FOR A TARGET ON ROUGH SUBSTRATE IN LAB EXPERIMENT

In this section we describe two basic radiative transfer models for explaining observed reflectance scattering at an angle θ from a contaminated rough surface when the sample is illuminated by a directional source (incidence angle θi). Section 3.1 presents the models, and Section 3.2 shows application of the model to laboratory data.

3.1   THEORY

We present two basic models (Equations 9 and 10) for the reflected radiance at angle θ from the contaminated surface: (a) for a scenario for which we neglect the contribution from reflection off the target's surface, hence we only account for the red and green rays in Figure 1, and (b) when we include reflection off the target's surface, hence we take into account the red, blue, and green rays (only neglect multiple scattering effects and the scattering portion of the target volume term). We prefer to use the simpler model due to better numerical properties (ease and stability of computation). However, in certain limiting cases the simple model breaks down, for instance, when the height of material is very large or when the underlying substrate is completely specular. In these cases, off-specular radiation can only originate from surface and volume scattering. Surface reflection is only incorporated into the second model.

Even though mathematically the simple equation breaks down in certain limiting cases, there is an equivalency (to be explained in the next section) that allows the simple model to still perform well. In our experience the simple first model is sufficient in analyzing the limited data available to us. Note also, that because even rough surfaces can be close to specular, the specular direction has a higher signal-to-noise ratio and is rich in spectral features. This is another reason why the first model may be sufficient in practice.

Neglecting reflection off the target's surface (blue rays in Figure 1) is justified when the underlying rough surface (e.g., aluminum) is much more reflective than the target (e.g., larger refractive indices for the surface) and the optical depth of the target is small. For a small optical depth, the contribution of scattering events within the target layer should be negligible compared with the contribution from the two-way attenuated incidence that penetrates the target. The

19

simpler model is preferable because it has fewer parameters to be solved for in the numerical optimization procedure.

3.1.1 *RADIATIVE TRANSFER MODEL WITHOUT TARGET'S REFLECTANCE CONTRIBUTION*

The reflectivity $R(\theta) = M(\theta)/L(\theta_i)$ of a contaminated surface at reflectance angle θ when the surface is illuminated with a strong directional source $L(\theta_i)$ and the reflectance from the target's surface is neglected is given by a linear mixture model (Equation 2) as:

$$\left\{ \begin{array}{l} R(\theta) = M(\theta)/L(\theta_i) = (1-f) \times R_0(\theta) + f \times R_0(\theta) \times e^{-h\left(\frac{1}{\cos(\theta_i)} + \frac{1}{\cos(\theta)}\right)(\alpha + g\Delta n)} \\ R_0(\theta) = \rho_0(n_0, k_0, \theta_i) \exp(a_0\lambda^{-2} + b_0\lambda^{-1} + c_0) \end{array} \right\} \tag{9}$$

where h is the *approximate* target thickness (see next paragraph for details), α is the target's absorption coefficient and the reflectance of the bare rough surface, $R_0(\theta)$, is given by Equation 3 as a function of the surface refractive indices (n_0, k_0) and the decay model fitting parameters (a_0, b_0, c_0), Δn is given by the Kramers-Kronig analysis as described in Section 2.1.3, and g is the "dispersion factor."

The exponential term in the first line of Equation 9 is the transmission, or two-way attenuation of photons through the target material and reflected off of the bare substrate, but it requires a more detailed explanation. First, the sum of inverse cosines represents the lengthening of the path due to a non-normal viewing geometry: incident photons propagate along θ_i to the substrate along the incident direction through the material; photons reaching the sensor reflect off of the substrate with a slant path through the material along the direction θ.

For specular geometry, $\theta = \theta_i$ and $h\left(\cos^{-1}(\theta_i) + \cos^{-1}(\theta)\right) \to 2h/\cos(\theta_i)$. The inverse cosine terms are only a first order approximation to the true path through the material, since the propagation direction through a medium is modified by the refractive index (through Snell's law) which is wavelength dependent. Computing the exact propagation in a medium where the imaginary refractive index, k, is not zero is problematic[12,23-25] because the propagation angle in the material is complex in an absorbing medium; mathematically this represents the *inhomogeneity effect*[23,25] where planes of constant phase and planes of constant amplitude in the electromagnetic wave lie in different directions.

If $\theta = \theta_i = 0$ (normal geometry), or if $n = 1$, then the transmission pathlength $h\left(\cos^{-1}(\theta_i) + \cos^{-1}(\theta)\right)$ is correct, and h can be interpreted as the height or thickness of the material. Otherwise, the cosine terms will not represent the correct propagation direction, and the value of h will have to compensate for this error. Therefore, the solution value of h given by the model may not be directly interpreted as the material thickness, although the combined term $h\left(\cos^{-1}(\theta_i) + \cos^{-1}(\theta)\right)$ will represent the average pathlength through the material (where the average is over wavelength). The materials of interest are conventional materials with $n \geq 1$ (the refractive index of the surrounding medium, air, is 1), and thus the lengthening of the path represented by $\cos^{-1}(\theta_i) + \cos^{-1}(\theta)$ will be an overestimate, and h will tend to underestimate the true material height. If n is not too much bigger than 1, and/or the incident and output angles are not too far removed from normal, the average path-error adjustment incorporated into h by the model fit will be small. Also, the quantity Δn (see Section 2.1.3) gives the change in refractive

index with wavelength (dispersion) referenced to a particular value. If $h\big(\cos^{-1}(\theta_i) + \cos^{-1}(\theta)\big)\alpha$ is the average optical depth through the material, then $h\big(\cos^{-1}(\theta_i) + \cos^{-1}(\theta)\big)\alpha + g\Delta n$ includes wavelength-dependent adjustments to the optical depth, where the g parameter controls the strength of the dispersion effect. We chose to write the term as $h\big(\cos^{-1}(\theta_i) + \cos^{-1}(\theta)\big)\big(\alpha + g\Delta n\big)$ instead so that $g\Delta n$ would disappear in the limit of $h \to 0$ (no target material present). Note that initially we were motivated to include the *gΔn* term for empirical reasons (it greatly improved the fit of the model applied to potassium chlorate data, see Section 3.2.1) before realizing the (qualitative) physical interpretation. We had also attempted to use the Yang and Liou[25] approach (which avoids complex propagation angles in Snell's law) to compute the wavelength dependent pathlength, however, the results were less good (with regard to fitting the data) than using the *gΔn* term.

The fact that the *gΔn* term is more effective raises the question, why? The *gΔn* approach qualitatively corrects for wavelength-dependent dispersion, but in a less rigorous way than the approach of Yang and Liou. The *gΔn* term may be compensating for other effects that are ignored in the simple model, for example, scattering by the target volume. Since the probability of scattering depends on the pathlength through the medium, and the *gΔn* term relates to the pathlength through the medium, the *gΔn* term may be able to approximate gains and losses due to scattering. Thus, although we do not include any terms to *explicitly* model the scattering contribution of the target volume effect (see Figure 1 and associated discussion in Section 1) we believe that the model implicitly has the ability to account (for some portion of) target-scattered photons. In light of this thought, it is natural to wonder if $\alpha + g\Delta n$ may be interpreted as the extinction coefficient, α_{ext}, and *gΔn* as the attenuation coefficient due to scattering, α_{scat}. However, immediately it can be seen that this cannot be the case, since physically $\alpha_{scat} \geq 0$ but *gΔn* may have both positive and negative elements. It is tantalizing, though, that there may be a connection between such a simple function *gΔn* and scattering, which usually requires complicated theories.

Another reason why only using *α* in the transmission term (instead of α_{ext}) is working well may be due to a balancing of energy. The absorption coefficient, *α*, overestimates the amount of transmission, but at the same time we neglect scattered photons within the material (some of which are compensated for by the *gΔn*). Therefore, the total error is smaller than might otherwise be expected.

We note that a paper by Toll,[26] which shows that a perfect filter cannot exist due to the constraint of causality, provides an interesting alternate interpretation of the *gΔn* term. When one frequency is absorbed by a filter all other frequencies are affected and phase shifts of all other frequencies must take place in order to comply with causality (i.e., no output can exist before an input occurred). The phase shifts ensure destructive interferences that will annihilate all output waveforms in the time domain for times prior to the input occurrence. An absorbing medium (e.g., the potassium chlorate target) can be viewed as a "filter" where some frequencies (wavelengths) are absorbed. Thus, following Toll's argument of "no ideal filter exists" other wavelengths must incur phase shifts. The mechanism to produce phase shift for wavelengths is with the refractive index that indeed force optical phase shifts (change in phase velocity and therefore path through the material). Thus, we interpret our function *gΔn* as being able to introduce the "proper" phase shifts.

We note that Equation 9, as written, goes to zero if $\theta \neq \theta i$ and the substrate is perfectly specular. In this case, off-specular photons can only come from target surface reflection and

volume effects that are ignored. In the volume scattering term, there are forward-scattered photons that change direction, and are specularly reflected by the smooth surface, but along a different direction. These photons are then measured as off-specular photons that were subject to two-way attenuation with a different pathlength through the material. Therefore, they can be thought of as if they were photons that were scattered by the rough surface instead of by volume scattering. This equivalence means that Equation 9 *can* numerically represent off-specular reflection even for smooth surfaces (demonstrated in Section 3.2.4).

A deficiency of Equation 9 is that when the target thickness is very large, the exponential term goes to zero (optical depth is proportional to thickness of the material), and thus $R(\theta) \xrightarrow{h>>>} (1-f) \times R_0(\theta)$, which is independent of the target. Thus, though this simple model is attractive it may not be applicable if there is too much material deposited on a substrate. To avoid this limitation, we add another term to Equation 9 include reflectance from the target, presented in the next section.

3.1.2 *RADIATIVE TRANSFER MODEL WITH TARGET'S REFLECTANCE CONTRIBUTION*

When the reflectance due to the target's surface (blue rays in Figure 1) is added to Equation 9 we obtain a slightly more complex radiative transfer model. We assume that the target can be viewed as a rough surface (see Figure 2) due to its complex morphology. Thus, we can conceptually model the reflectance of the target, R_t, using Equation 3) and target refractive indices (n,k). The radiative transfer model becomes,

$$\left\{ \begin{array}{l} R(\theta) = (1-f) \times R_0 + f \times \left(R_t + (1-R_t)R_0 \times e^{-h\left(\frac{1}{\cos(\theta_i)} + \frac{1}{\cos(\theta)}\right)(\alpha + g\Delta n)} \right) \\ R_0 = \rho_0 \exp(a_0 \lambda^{-2} + b_0 \lambda^{-1} + c_0) \\ R_t = \rho_t \exp(a_t \lambda^{-2} + b_t \lambda^{-1} + c_t) \end{array} \right\} \quad (10)$$

This simple radiative transfer model includes the contribution from the target's surface but does not include scattering contributions from *within* the target (although the discussion regarding an equivalence between forward scattered photons and transmitted photons—and the presence of the *g∆n* term—may allow some portion of the within-target scattering to be accounted for). To explicitly model scattering within the target one needs to employ scattering functions, a difficult task that involves information on shape and size of the target's particles. We chose to keep the model as simple as possible. Note that when $R_t \to 0$, Equation 10 → Equation 9. This model is appropriate for off-specular angles $(\theta \neq \theta_i)$ as well as for specular angles $(\theta = \theta_i)$.

The parameter set $\eta = \{f, h, g, a_0, b_0, c_0, a_t, b_t, c_t\}$ are unknowns to be solved for (discussed in the next section) and are scalars. The model inputs (α, n, k, n_0, k_0) and the data, R, are spectral vectors.

3.1.3 *SOLUTION OF THE RADIATIVE TRANSFER MODEL*

The objective of the model is to explain observed reflectance data with an emphasis on representing the spectral fingerprints of the target of interest. We wish to solve for the optimal set of parameter values (the *solution*), η, such that the model output and the observed reflectance data are identical. The number of spectral bands (typically >100) is greater than the number of unknowns (6 parameters in the case of Equation 9 and 9 parameters in the case of Equation 10); therefore, we have an overdetermined system of *nonlinear* equations. However, due to noise and model errors the system of equations is inconsistent and must be solved in a least squares sense. Consequently, applying the model is a problem of multivariable nonlinear function minimization.

There are many numerical routines that can be applied[27-28], however, the problem is hard suffering from the presence of local minima, saddle points, numerical instability, ill-conditioning, and non-uniqueness; these problems are more troublesome as the number of unknowns increases (the "curse of dimensionality"). Results are dependent on the solution method and the starting point (the initial solution). The problem is made more difficult if the expected physical constraints on the parameter values are applied: the fill factor should satisfy *0 $\leq f \leq$ 1*; the height, *h*, should be positive but attain a "reasonable" value (e.g., submicron range for potassium chlorate contamination $d_s < 100 \ \mu g/cm^2$); and the decay terms should satisfy $0 < D \leq 1$ and $0 < D_s \leq 1$ (see Section 2.1.3). Failing to obtain a physical solution puts in question the validity of the model, but even non-physical parameter values do not necessarily invalidate the results of the radiative transfer model. A non-physical parameter set means that solution values are not interpretable (e.g., if the solution value $h < 0$, then clearly it cannot be viewed as the thickness of the material) but may suggest that the model is too simple (e.g., in the case of $h < 0$ it could be that the model is approximating terms that are ignored such as surface reflection or volume scattering from the target when using Equation 9) or that there is error in the input values. An equivalent or better solution where the physical constraints are imposed may exist, but just not found by the numerical optimization routine. In addition, there is a relationship between the variables where, for example, an increase in *h* can be compensated for (somewhat) by decreasing *f*. These types of interrelations contribute to the mathematical non-uniqueness in the radiative transfer model.

We note that if reliable auxiliary measurements or a priori information is available, it may be possible to fix some parameters at known values, and optimize over a smaller subset of the parameter set, η. For example, with reliable H_0 measurements, *R(θ | f = 0)*, roughness coefficients (a_0, b_0, c_0) could be found that would allow only optimizing the parameter subset {*f, h, g*} (in the case of Equation 9). However, due to the potential non-uniformity of rough surfaces (see Section 2.2.6) it may be wiser to simply use these values to populate the initial solution, and optimize over the full parameter set. A priori information (such as height *h* being less than a micron) can be incorporated into bound constraints applied to the solution.

We used two numerical methods for solving the radiative transfer model: *fminsearch* (a built-in MATLAB function that uses the Nelder-Mead simplex algorithm[29]), and we implemented an optimization package based on the Newton-Raphson method. In the Newton-Raphson method bound constraints on the parameter set, η, may be applied in the optimization procedure to ensure physical values for *f* and *h,* or to limit the range of any of the parameters; *fminsearch* is an unconstrained method. We also attempted to use the constrained version of *fminsearch* (called *fmincon*, from MATLAB's optional Optimization Toolbox), but it did not perform as well.

3.2 RESULTS

In this section we present results of applying the model to lab-measured reflectance data. There are many ways one can quantify the goodness of fit between the model and the data. We chose two figures of merit: (a) *rms* least-squares error and (b) a matching angle, *ψ*, between the model and the data spectral vectors. In many detection algorithms[7] (e.g., a matched filter) the algorithm's performance depends on an angle between the two vectors (usually computed in a weighted coordinate system with a specified origin). If the angle is small, the measurements are labeled as H_1 (target is present). The ideal detection performance is for $\psi \rightarrow 0°$.

We compute the *rms* error metric from all wavenumbers (600-4000 cm^{-1}), thus it is a good indicator of overall model fit. Unless otherwise noted, the matching angle, *ψ*, is computed only from 750-1200 cm^{-1}, which overlaps the LWIR spectral region. This is more attuned to the identifying features of potassium chlorate, and thus *ψ* is a better metric for assessing detection/identification performance than *rms* error. For computing *ψ*, we used an unweighted coordinate system where the origin is given by the model-predicted H_0 spectrum, which is the spectrum that the model predicts when setting $f = h = g = 0$. In most cases, the *rms* error metric and *ψ* are noted directly in the figures.

3.2.1 *POTASSIUM CHLORATE ON ROUGH ALUMINUM*

We employed our simple radiative transfer model, Equation 9, for both specular and off-specular reflectance measurements of potassium chlorate on rough aluminum, using both $α_{pellet}$ and *α* as inputs. For specular angles, the use of Equation 9 is justified because of the very thin target (<1 μm) and the high reflectivity of the aluminum surface (applying Equation 10 gives nearly identical results; this suggests that target-surface reflectance is negligible). Figures 11-13 show the results for specular angles; solution values for the model parameters are summarized in Table 1.

Figure 11 shows model results for $\theta = \theta_i = 60°$ for two different concentration densities of potassium chlorate and using $α_{pellet}$ and *α* as inputs to the model (see caption). The potassium chlorate features point down, indicating that there is an attenuation or loss of energy due to the presence of potassium chlorate on the highly reflective underlying aluminum substrate. The major feature, composed of a double peak around 970 cm^{-1}, is fit fairly well in all cases, even by $α_{pellet}$ (which does not reflect the morphology of the target), but using *α* (from Figure 7) markedly improves the spectral shape, allowing the model to fit the double peak. Visually, the fit for the 50 and 100 μg/cm^2 samples are about the same with respect to $α_{pellet}$, though the *rms* and *ψ* metrics show that the 50 μg/cm^2 sample is a better fit. Using *α* improves both the 50 and 100 μg/cm^2 samples, but the improvement is much more significant for the 50 μg/cm^2 sample. This is not surprising, since *α* was derived from a 50 μg/cm^2 sample and it should be more attuned to the morphology of the 50 μg/cm^2 deposition. Nonetheless, using *α* is still an improvement for 100 μg/cm^2 in comparison to $α_{pellet}$.
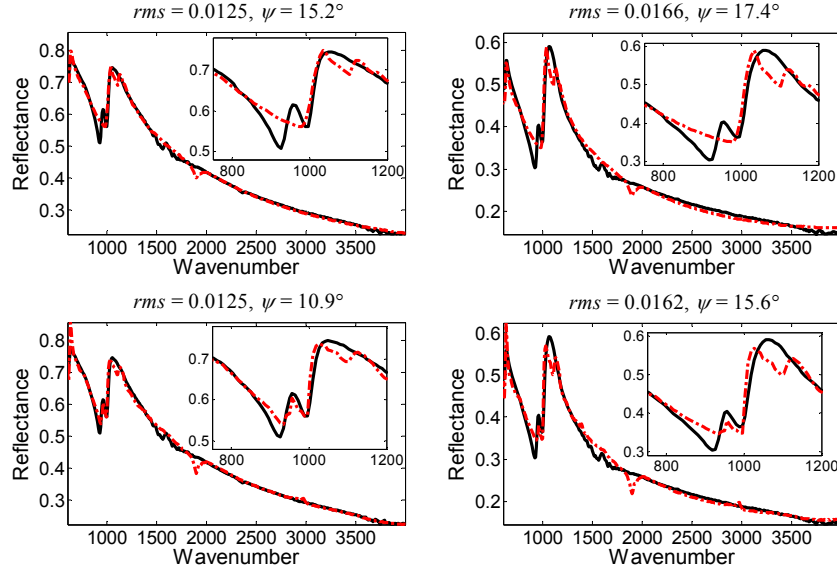
Figure 11. Model results (data in solid black, model in dashed red) applied to specular reflection measurements (60° incidence) of potassium chlorate deposited on rough aluminum at 50 µg/cm² (left column) and 100 µg/cm² (right column). Top row: model results using α_{pellet}. Bottom row: model results using α derived from a 50 µg/cm² sample.

Insets for figure show the response from 750-1200 cm^{-1}, which overlaps the LWIR region. Using α improves the fit, especially with regard to the double peak (between 900 and 1000 cm^{-1}) observed in the data. The potassium chlorate feature at 1900 cm^{-1} (that was used in the calibration procedure, Section 2.2.3) is stronger in the model output than in the measured reflectance; only a slight trace of this feature is observed in the data. This was consistently observed: integrating sphere measurements showed the feature at 1900 cm^{-1}, whereas in the ellipsometer the feature was suppressed. We do not have an explanation for this, though it may be a scattering phenomenon (losses in the integrating sphere are due to absorption, whereas losses in the ellipsometer measurements are due to extinction).

Figure 12 is similar to Figure 11, but the model is applied to specular reflection from the 50 µg/cm² sample at two different incident angles (45° and 32°). The model representation of the double peak around 970 cm^{-1} seems to have improved even further over as the incident angle becomes closer to normal (ψ gets smaller as the incident angle is reduced). We note that the integrating sphere reflectance measurements are for 8° incidence (near normal), and so the improvement in the fit as the incident angle is reduced may be because of an increased correspondence to the integrating sphere geometry.
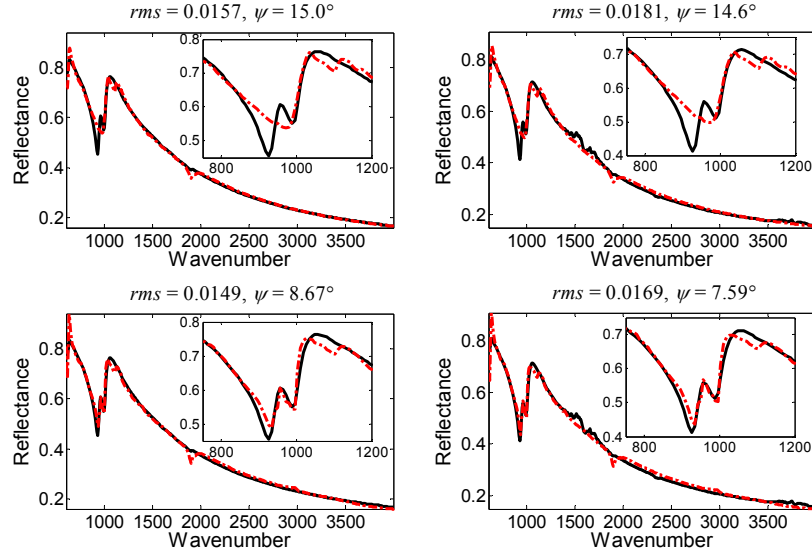
Figure 12. Model results (data in solid black, model in dashed red) applied to specular reflection measurements of potassium chlorate deposited on rough aluminum for 50 μg/cm² at 45˚ incidence (left column) and 50 μg/cm² at 32˚ incidence (right column). Top row: model results using α_{pellet}. Bottom row: model results using α derived from a 50 μg/cm² sample. Model representation of the spectral features improves as θ_i is reduced.

In Figure 13, we show results of the model applied to the same data as in Figure 12; however, the g parameter was forced to be zero. This removes the ability for the model to correct for path or implicitly model some scattering phenomena.
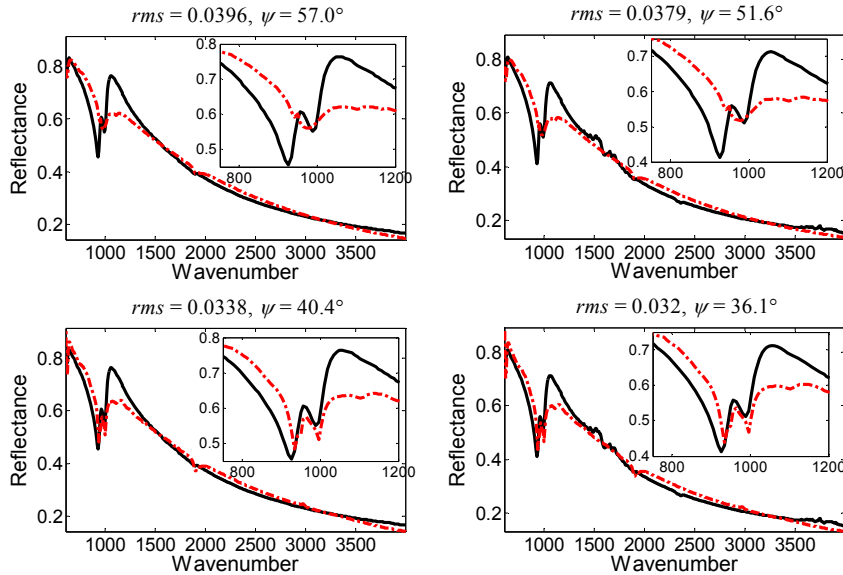
Figure 13. Same data as Figure 12, except the *g* parameter is constrained to be zero; thus the effects of dispersion are not present in the model. Comparison to Figure 12 shows that the *g* parameter plays a very important role in improving spectral fit to the data.

Since dispersion relates to pathlength through the material, and scattering is proportional to pathlength, inclusion of the $g\Delta n$ term ($g \neq 0$) may implicitly capture some of the volume

scattering effects from the target material (see Section 3.1.1). Model fits to the data are severely reduced for both α_{pellet} and α. The relative drop in performance of the model without the $g\Delta n$ function is much larger than the drop in performance if α_{pellet} is used instead of α. For potassium chlorate, the dispersion function appears vital in order to achieve good performance. Note that a contrasting observation will be made with regards to ammonium nitrate (see Section 3.2.2).

Table 1 summarizes the solution parameters for the model applied to specular measurements, using α. The value of h, the approximate height of the target layer, is shown after dividing by 10, which accounts for the order-of-magnitude discrepancy discussed in Section 3.2.3. For display purposes, the values of g, a_0, and b_0 are also scaled, as noted in the table. It is noteworthy that the estimated target thickness for d_S = 50 µg/cm^2 and h = 0.51µm agrees with the *a priori* estimate (Section 2.2.4), and additionally is *consistently predicted by the model independently of the incident angle*. The fill factor is in the expected range, and increases with decreasing incident angle. This may be due to obscuration of target material due to roughness of the aluminum substrate; as the incident angle becomes closer to normal, the sensor "sees" deeper into the canyons and valleys of the substrate, making more target material visible. Note that one could also expect the fill factor to *decrease* with increasing incident angle due to the sensor seeing deeper into canyons and valleys of the target, making more "bare" substrate visible. Which factor dominates will depend on the roughness scale of the two materials and the nature of the deposition.

Table 1. Solution values for fitting specular reflectance measurements of potassium chlorate on rough aluminum, using α.

d_s	θ_i	θ	f	$h/10$ [1]	g [2]	(a_0, b_0, c_0) [3]
50 µg/cm^2	60°	60°	0.24	0.51 µm	19.4	(6.96, -6.98, 0.25)
	45°	45°	0.38	0.51 µm	12.5	(7.70, -8.60, 0.45)
	32°	32°	0.45	0.51 µm	9.69	(9.28, -9.47, 0.47)
100 µg/cm^2	60°	60°	0.27	0.79 µm	33.9	(12.9, -9.65, 0.053)

[1] h is displayed divided by 10 to account for the order-of-magnitude discrepancy (see 3.2.3) .

[2] g is displayed after multiplying by $(h/10)\times 1\cdot 10^{-3}$ and by $\cos^{-1}\theta_i + \cos^{-1}\theta$.

[3] Roughness parameters a_0 and b_0 are shown multiplied by scaling constants $1\cdot 10^8$ and $1\cdot 10^4$, respectively.

The product $f\times h$ is proportional to the mass per unit area predicted by the model. For the same incident angle, the model should predict a value of $f\times h$ for 100 µg/cm^2 that is twice the value for 50 µg/cm^2. The model is close: the ratio is only a little less than 2 at 1.74. For the three different specular angles at d_S = 50 µg/cm^2, the model sees a greater mass of target material as the incident angle gets closer to normal; evidently there is more signal from potassium chlorate as the incident angle is reduced. This can be verified through inspection of Figures 11 and 12, where the modulation depth of the main potassium chlorate feature increases with decreasing incident angle. This trend suggests that, if given a choice, a smaller incident angle should be preferred. We had already concluded that the model fit improved with decreasing incident angle. Thus, not only is there more signal, but the signal is also fit better as the incident angle is reduced. Finally, although we do not have a clear interpretation of the values for the parameters g, a_0, b_0, and c_0, it is encouraging that all show a monotonic trend with decreasing incident angle. This suggests that a more controlled experiment could be designed to determine a useful empirical relationship of these parameters to the characteristics of the sample.

Applying the model to off-specular reflectance data is more challenging. There is much less energy observed from the rough aluminum at off-specular angles, and a much lower signal-to-noise ratio in the data. The potassium chlorate feature at ~970 cm^{-1} appears in the off-specular reflectance data with similar shape, but it is not intense, and it points up instead of down: there is an *addition* of energy due to the presence of the potassium chlorate on the substrate. This is an indication that the two-way attenuation term is not the dominant effect contributing to the measured reflectance, and that volume scattering effects or surface reflection from the potassium chlorate (or both) are significant. However, as discussed in Section 3.1.1, we think that the two-way attenuation term can approximate effects that are ignored by the model. Therefore, we applied both Equations 9 and 10 to the off-specular data. Note that Equation 9 only includes the two-way attenuation term; in order to produce potassium chlorate peaks in the correct polarity, Equation 9 must produce a negative (non-physical) value for either f or h. Equation 10, since it includes a term for the reflectance from the target surface, has the potential to produce physical values for f and h. Surprisingly, we observed better results using Equation 9 than Equation 10. Partially this is due to the numerical difficulties of fitting the more complicated model: Equation 9 is a special case of Equation 10, and so any solution found by Equation 9 can also be found by Equation 10. Additionally, it may be indicative that reflectance from the target surface is still negligible (even in the off-specular geometry), since explicitly including the surface-reflectance term in Equation 10 did not result in an improved fit. Because we observed better performance from Equation 9, we only present results using the simpler model.

A typical example using Equation 9 is shown in Figure 14, for 50 µg/cm^2 and angles θ_i = 45°, θ = 41°. The left plot shows the data and model fit when all wavenumbers are used, and α is used in the model. The model converges to a poor solution. In the right plot, only wavenumbers less than 1200 cm^{-1} are used to fit the model. This improves the quality of the fit around the potassium chlorate feature between 900 and 1000 cm^{-1}, showing that even the simple model can represent the off-specular reflectance signatures from the target. However, because larger wavenumbers did not contribute to the model fit, the results beyond 1200 cm^{-1} suffer (not shown, but reflected in the increased value of the *rms* error statistic).
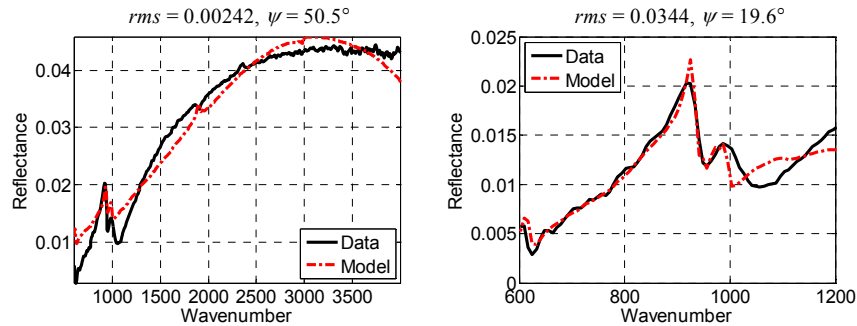
Figure 14. Model results applied to off-specular reflection (θ_i = 45°, θ = 41°) from a 50 µg/cm^2 potassium chlorate sample. *Left:* all wavenumbers are used to fit the model. *Right:* only wavenumbers smaller than 1200 *cm*$^{-1}$ are used to fit the model.

An alternative procedure is motivated by the fact that the rough aluminum substrate is highly specular and that the off-specular reflectance is so small. Let the specular reflection be denoted $R(\theta_i)$, and the off-specular measurement be denoted $R(\theta_j)$, with the understanding that $\theta_j \neq \theta_i$. The quantity $1 - R(\theta_j)$ is all the energy from all other reflectance angles, including the

specular angle; however, the majority of the energy is from the specular angle, and thus $1 - R(\theta_j) \approx R(\theta_i)$ is qualitatively similar to a specular reflectance spectrum.
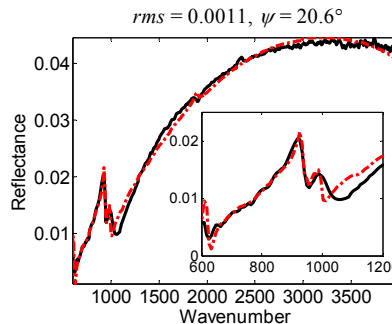
Figure 15. Model (fit using the alternative procedure) results applied to off-specular reflection (θ_i = 45°, θ = 41°) from a 50 µg/cm^2 potassium chlorate sample.

The alternative procedure circumvents some numerical issues in fitting the model to off-specular reflectance spectra and improves both the *rms* error and the matching angle, ψ. In our experience, specular reflection spectra are robustly fit by the model, without the need of limiting the spectral range. Therefore, an alternative procedure is to apply the model to the "pseudo-specular" reflection measurement $1 - R(\theta_j)$. The output radiance of the model, $\hat{R}$, may be converted back into the domain of the original off-specular reflectance measurement by computing $1 - \hat{R}$. The results of this procedure are shown in Figure 15. The resulting fit parameters are physical (*f* and *h* are non-negative, and $f < 1$), however, it is not clear how to interpret these parameters since they are related to $1 - R(\theta_j)$. The overall quality of the fit is much improved (*rms* value in Figure 15 is smaller than those in Figure 14). The representation of the potassium chlorate feature has also been improved, with a smaller value of the matching angle, ψ, compared to the left plot in Figure 14 (50.5°→20.6°). It is encouraging that such a simple model can successfully represent both specular and off-specular reflectance data of a contaminated rough surface.

3.2.2 *AMMONIUM NITRATE ON ROUGH ALUMINUM*

Results of the model (Equation 9) applied to ammonium nitrate at 50 µg/cm^2 at $\theta = \theta_i = 60°$ are shown in Figure 16. Unlike for potassium chlorate, incorporating the effects of morphology by using α (derived from a 50 µg/cm^2 sample on rough aluminum, see Figure 8) does *not* help improve the results of the model over using α_{pellet}. Figure 16 also shows model results when the *g* parameter was constrained to be zero. The figure shows that the *gΔn* function does not significantly improve the quality of the match (also unlike potassium chlorate). We do not have an explanation for the differences in behavior between potassium chlorate and ammonium nitrate.

$rms = 0.00957$, $\psi = 13.9°$

$rms = 0.0138$, $\psi = 24.6°$
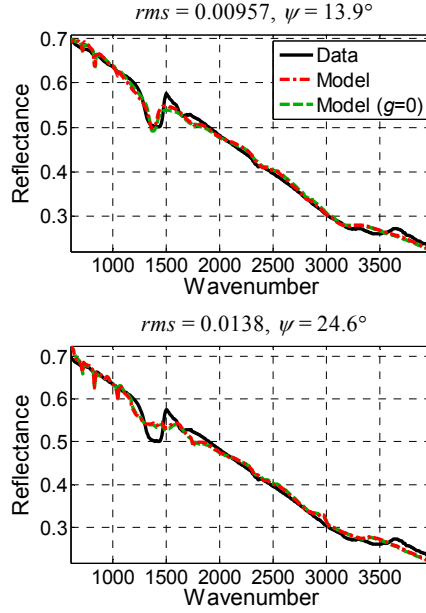
Figure 16. Model results (data in solid black) applied to specular reflection measurements for 60˚ incidence of ammonium nitrate deposited on rough aluminum at 50 µg/cm². *Top*: model results using α_{pellet}. *Bottom*: model results using α derived from a 50 µg/cm² sample.

     Two model curves are shown in each plot: green gives the model result when the g parameter is constrained to equal zero, red is the unconstrained model. In contrast to the potassium chlorate results, any improvement in fitting associated with the g parameter is very slight. Also contrary to potassium chlorate, α_{pellet} gives better results than α. Note that the main feature of ammonium nitrate that is being fit by the model is at 1400 cm⁻¹. This is on the edge of the LWIR atmospheric window and (a) may be masked by H_2O absorption, and (b) is at a region of higher sensor noise due to poorer responsivity of MCT detectors typically used in remote sensors. Thus, in practice this feature may not be a reliable one for detection or identification purposes in the LWIR. Other spectral features due to ammonium nitrate are much weaker. These observations illustrate that ammonium nitrate is likely to present a more difficult detection problem than potassium chlorate. Note that for ammonium nitrate, we computed the matching angle, ψ, over the 1000-1500 cm⁻¹ range.

     Off-specular reflection measurements are well fit by the model, as shown in Figure 17, even for *extremely* low signal (right plot, $\theta_i = 60°$, $\theta = 52°$). The behavior of the off-specular reflectance for ammonium nitrate is another contrasting point in comparison to potassium chlorate. For potassium chlorate the off-specular spectral shape looked similar to a mirror image of the specular reflectance spectrum (features appeared in the opposite polarity). For ammonium nitrate, the spectral shape of the off-specular and specular reflectance spectra are qualitatively the same, with spectral features appearing in the same polarity. This suggests that even for off-specular angles, the two-way attenuation term is sufficient for modeling the data, and surface and volume scattering effects are likely negligible. In Figure 17, the signal-to-noise is particularly low, and yet the spectral features are still visible and fit quite well.
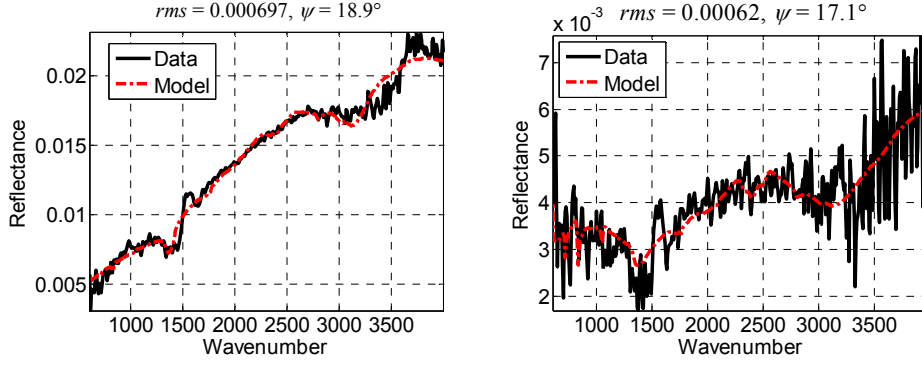
Figure 17. Model results (data in solid black, model in dashed red) applied to off-specular reflection measurements of ammonium nitrate deposited on rough aluminum at 50 *μg/cm*^{2}. *Left*: θ = 60° and θ = 54°. *Right*: θ_i = 60° and θ = 52°; both plots show results using α_{pellet}.

Solution values for the model results are summarized in Table 2.

Table 2. Solution values for fitting ammonium nitrate on rough aluminum, using α_{pellet}.

d_s	θ_i	θ	f	$h/80$ [(1)]	g [(2)]	(a_0, b_0, c_0) [(3)]
50 μg/cm^2	60°	60°	0.21	0.15 μm	20.0	(-3.67, -1.82, -0.17)
		54°	0.35	0.13 μm	9.16	(-14.9, 10.8, -5.79)
		52°	0.32	0.43 μm	-72.2	(-3.74, 3.82, -5.98)

[(1)] h is displayed divided by 80 to account for the magnitude discrepancy (see 3.2.3) .

[(2)] g is displayed after multiplying by $(h/80)\times1\cdot10^{-3}$ and by $\cos^{-1}\theta_i + \cos^{-1}\theta$.

[(3)] Roughness parameters a_0 and b_0 are shown multiplied by scaling constants $1\cdot10^8$ and $1\cdot10^4$, respectively.

3.2.3 *MODEL SPECIFICITY*

The simple model (Equation 9) produced good results on both potassium chlorate and ammonium nitrate samples (Figures 11-17). However, with enough fitting parameters in a model one can achieve good fit for any given data. Thus, the question of specificity of the model needs to be demonstrated. For example, will the fit be good if we assume that the target in the measurements is ammonium nitrate instead of being potassium chlorate?

In Figure 18 we applied the model to both potassium chlorate and ammonium nitrate reflectance spectra but took the spectral signature from the wrong material, i.e., for the potassium chlorate data, the absorption coefficients of ammonium nitrate were used, and vice versa. The model fit is extremely poor in both cases, and thus it is unlikely these two materials will be misidentified as one another.

$rms = 0.033, \psi = 60.1°$ (left)

$rms = 0.0188, \psi = 83.7°$ (right)
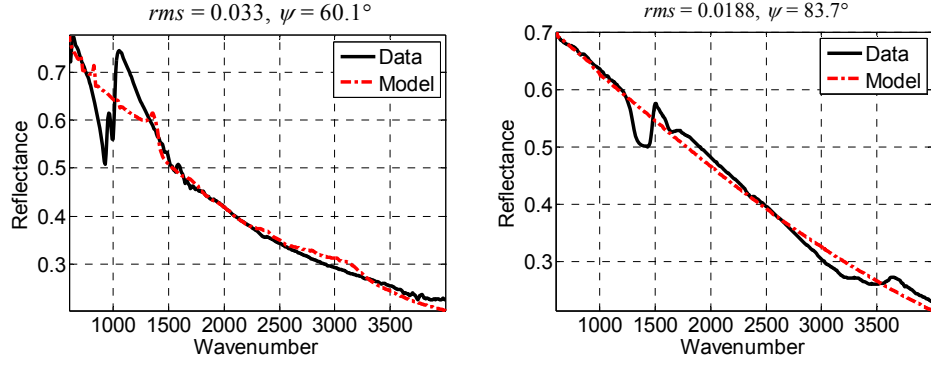
Figure 18. Specificity of the model. Left: Reflectance data of potassium chlorate deposited on rough aluminum at 50 µg/cm², where α and Δn used in the model are incorrectly taken for ammonium nitrate. Right: Reflectance data is for ammonium nitrate deposited on rough aluminum at 50 µg/cm², where α and Δn used in the model are incorrectly taken for potassium chlorate.

3.2.4 *POTASSIUM CHLORATE ON ALUMINUM MIRROR*

Potassium chlorate was deposited on a smooth aluminum surface at 100 and 400 µg/cm². Figure 19 shows specular reflection measurements at 60˚ incidence for these two samples (left column is 100 µg/cm², right column shows 400 µg/cm²) along with model results using α_{pellet} (top row) and α (bottom row). Off-specular reflectance of the potassium chlorate on the mirror was qualitatively similar to potassium chlorate on rough aluminum; hence, off-specular results for the mirror surface are not presented.

$rms = 0.0311, \psi = 13.1°$ (top left)

$rms = 0.0388, \psi = 14.5°$ (top right)

$rms = 0.0353, \psi = 12.0°$ (bottom left)

$rms = 0.0394, \psi = 12.4°$ (bottom right)
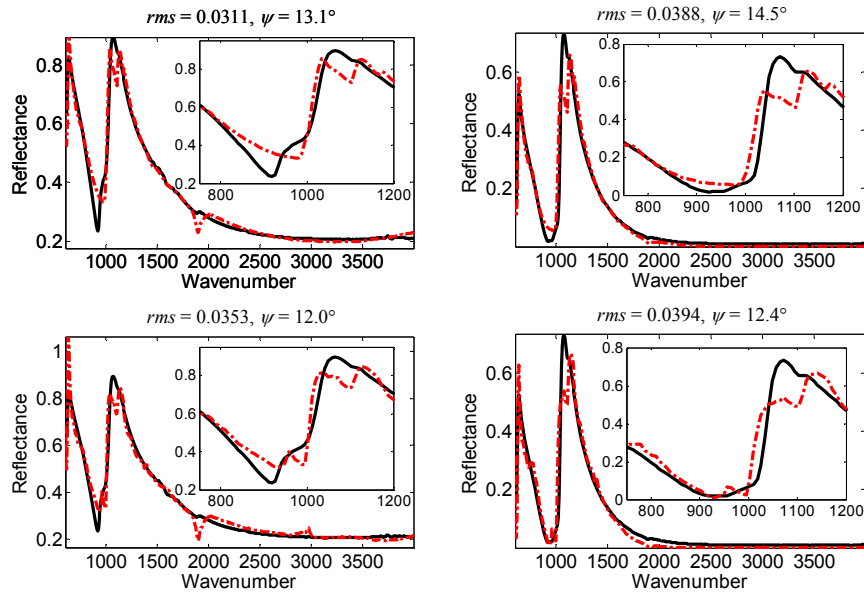
Figure 19. Model results (data in solid black, model in dashed red) applied to specular reflection measurements of potassium chlorate at 100 µg/cm² (left column) and 400 µg/cm² (right column) at 60˚ incidence. *Top row*: model results using α_{pellet}. *Bottom row*: model results using α derived from the 50 µg/cm² sample.

The left row of Figure 19 is for an identical deposition procedure and surface density and incidence angle as the right column of Figure 11; the only difference is the roughness of the substrate. The potassium chlorate feature shows slight differences between the two plots: on

32

rough aluminum (Figure 11), there is a clear double peak at 920 and 990 cm^{-1}. On the aluminum mirror (Figure 19) the double peak is not resolved; the peak at 990 cm^{-1} appears only as a slight shoulder. This illustrates the impact of the surface upon which the contamination lies to the measured reflectance. Neither α_{pellet} nor α (derived from 50 µg/cm^2 on rough aluminum) perfectly recreate the observed spectral shape of the potassium chlorate on the aluminum mirror: α_{pellet} cannot represent the shoulder whereas the double peak produced by α is too resolved. Thus, for *optimal* performance, optical signatures (absorption coefficients) should be measured for similar deposition *and* substrate characteristics. That being said, the differences in shape are not extreme, the quality of the fit (for both α_{pellet} and α) is good, and thus a signature library derived only from different depositions may give *sufficient* performance. For the 400 µg/cm^2 deposition (right column of Figure 19), the potassium chlorate feature has begun to saturate, broadening the peak and making the effects of the double peak (the shoulder) less apparent.

Table 3 summarizes solution parameters for the model.

Table 3. Solution values for fitting potassium chlorate on aluminum mirror, using α.

d_s	θ_i	θ	f	$h/10$ [(1)]	g [(2)]	(a_0, b_0, c_0) [(3)]
100 µg/cm^2	60°	60°	0.56	0.84 µm	27.2	(26.6, -16.4, 0.99)
400 µg/cm^2			0.99	1.10 µm	21.0	(-306, 45.7, -2.07)

[(1)] h is displayed divided by 10 to account for the order-of-magnitude discrepancy (see 3.2.3) .

[(2)] g is displayed after multiplying by $(h/10)\times 1\cdot 10^{-3}$ and by $\cos^{-1}\theta_i + \cos^{-1}\theta$.

[(3)] Roughness parameters a_0 and b_0 are shown multiplied by scaling constants $1\cdot 10^8$ and $1\cdot 10^4$, respectively.

It is interesting to compare to Table 1 (potassium chlorate on rough aluminum). The values of h and g for 100 µg/cm^2 are similar between the rough aluminum and aluminum mirror substrates. On the aluminum mirror, the model predicts a larger fill factor, and a larger $f\times h$ product (proportional to target area-density predicted by the model). This is indicative that there is more signal from potassium chlorate on the mirror than the rough substrate, a fact that may be verified by inspecting the modulation depth of the potassium chlorate feature in Figures Figure 11 and Figure 19. Observing more signal is probably related to the larger reflectivity at the specular angle of the smooth aluminum mirror compared to the rough aluminum. This suggests that it may be more likely to detect signatures from contaminants on smoother and/or more highly reflective substrates.

3.2.5 *POTASSIUM CHLORATE ON PAINTED ROUGH ALUMINUM SUBSTRATE*

Potassium chlorate was deposited on a black painted aluminum surface at 50 µg/cm^2 and 100 µg/cm^2. We did not know much about this substrate (n and k were not available) and thus, we had some choices on how to apply the model: (a) assume maximal ignorance, using Fresnel reflectance of $\rho_0 = 1$, and allow the decay function to fit the (smooth portions) of the underlying reflectance. With this method, any spectral features in the underlying substrate will not be explainable by the model, but the fit of the identifying chemical features (from the target) may still be good enough for identification. (b) Use an auxiliary measurement of reflectance of the painted substrate as a substitute to the known Frensel reflectance. We had available a total reflectance measurement obtained from the integrating sphere. This is not for the same geometry as the directional reflectance measurement, but we will assume that ρ_0 (Fresnel reflectance) for the particular incident angle is not too far from the measured total reflectance, and we will let the decay function modify the spectral shape in an attempt to achieve a better fit. The hope is that this procedure will better explain spectral features that appear in the

reflectance measurement that are due to the substrate. Note, that this is *not* the same as taking measurements of the H_0 condition and using them *directly* (because the decay term allows modification). This might compensate for the fact that the H_0 (bare substrate) has an intrinsic variability (see Section 2.2.6).

Figure 20 shows model results for the 50 μg/cm^2 (left column) and 100 μg/cm^2 (right column) depositions at $\theta = \theta_i = 60°$ using both α_{pellet} and α, using the first option, above (setting ρ_0 = 1 in the model due to lack of knowledge regarding the substrate). Measured reflectance values are small (less than 0.15) indicating that the black painted surface is not very reflective; there are several sharp features in the 1200-1800 cm^{-1} range that are attributable to the substrate. Spectral features due to the painted substrate are evident in the 1200-1800 wavenumber range. Despite not using any specific information about the substrate, the potassium chlorate feature near 1000 cm^{-1} is fit fairly well by α_{pellet} and α, but the feature points up; it is the opposite polarity in contrast to Figures Figure 11, Figure 12, and Figure 18.
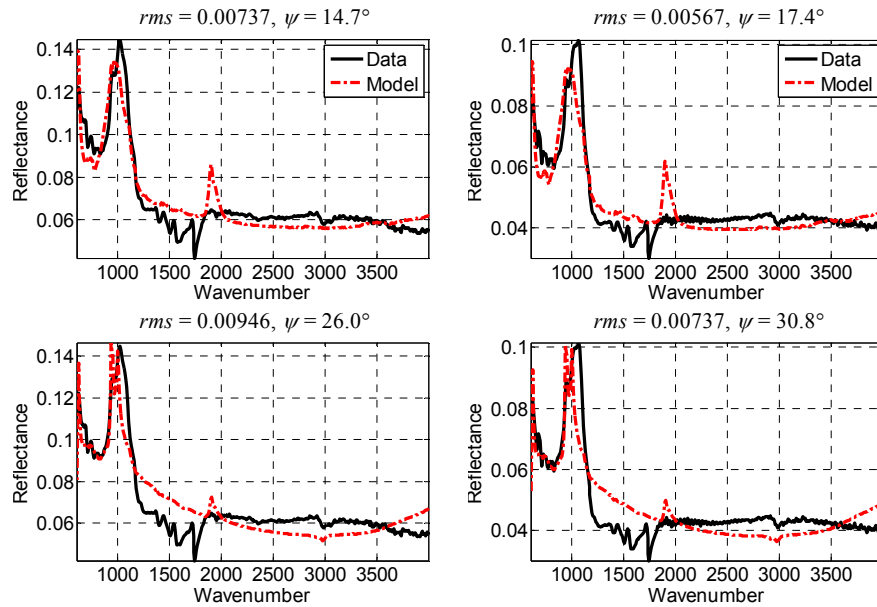
Figure 20. Model results (data in solid black, model in dashed red) applied to specular reflection measurements of potassium chlorate deposited on painted aluminum at 50 μg/cm^2 (left column) and 100 μg/cm^2 (right column), assuming that the Fresnel reflectance from the substrate, ρ_0, is 1. *Top row*: model results using α_{pellet}. *Bottom row*: model results using α derived from the 50 μg/cm^2 sample.

There is an addition of energy because of the presence of the potassium chlorate, overall it is more reflective than the underlying substrate. In one regard the poor reflectivity of the substrate is problematic for the model: not many transmitted photons that interact with the substrate will reflect back to the sensor, R_0 times the two-way transmission term will be small, and it is less likely that the volume scattering term (and the surface reflection term, in the case of Equation 9) will be negligible. However, as discussed in Section 3.1.1, we think that the two-way attenuation term can approximate effects that are ignored by the model. Evidently this is true, as indicated by the good fits to the potassium chlorate feature obtained in Figure 20, which used Equation 9. Note, however, that Equation 9 necessarily must result in *h* or *f* to be negative (non-physical) in order to produce peaks in the observed polarity. Equation 10, since it includes a term that directly models the reflectance from the surface of the potassium chlorate, has the

potential to produce features with the correct polarity without resorting to non-physical parameters. We will discuss the differences between Equations 9 and 10 applied to the painted aluminum substrate shortly, but first we will turn to the second option in modeling the substrate.

Figure 21 is identical to Figure 20, except that an auxiliary reflectance measurement of the bare painted aluminum substrate is used in lieu of the Fresnel reflectance. The features in the 1200-1800 cm^{-1} range are now excellently fit by model, and the fit to the main potassium chlorate feature around 1000 cm^{-1} is improved slightly as well. The fit beyond 1800 cm^{-1} is poor, evidently there is a difference in spectral shape between the auxiliary reflectance measurement and the observed reflectance of the substrate over this range. Note that α_{pellet} and α visually appear about equally well-suited for representing the spectral shape of the potassium chlorate on painted aluminum; the ψ metric shows that α_{pellet} is better.
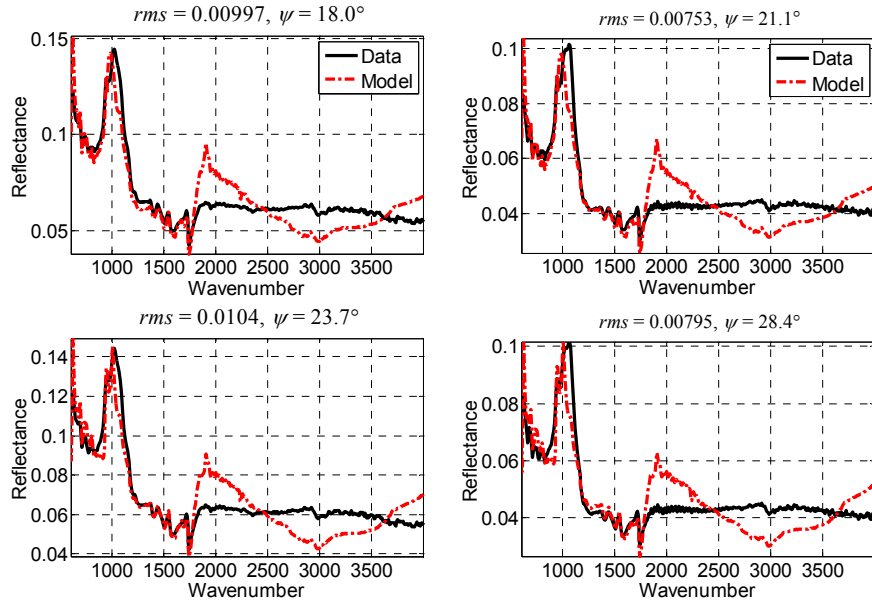

Figure 21. Model results (data in solid black, model in dashed red) applied to specular reflection measurements of potassium chlorate deposited on painted aluminum at 50 µg/cm^2 (left column) and 100 µg/cm^2 (right column), except that the Fresnel reflectance term, ρ_0, is taken from an auxiliary integrating sphere reflectance measurement of the bare painted aluminum substrate.
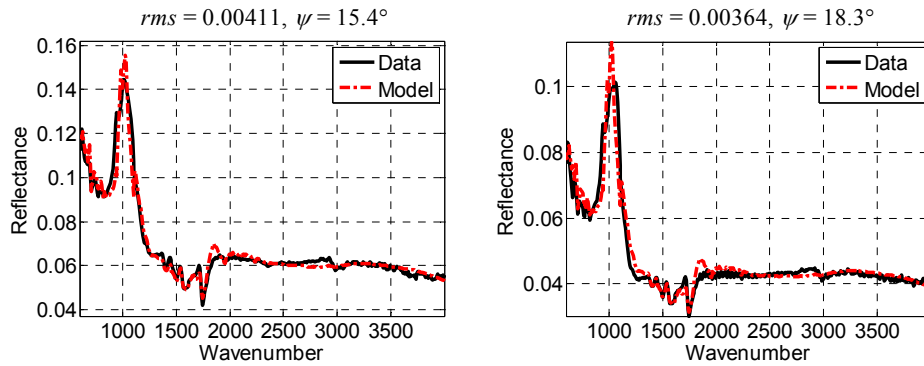
Figure 22. Identical to top row of Figure 21, except Equation 10, which is the more complicated model that includes reflectance from the surface of the target is used, instead of Equation 9.

As discussed above (and in Section 3.1) it is expected that Equation 10 will be a more physically appropriate model when the substrate is not very reflective. Comparing Figure 22 to the top two plots of Figure 21, the fits using Equation 10 are as good or better than those using Equation 9. But more importantly, the parameter estimates using Equation 10 are positive (f = 0.16 and h = 1.40 µm for 50 µg/cm^2 and f = 0.17 and h = 1.26 µm for 100 µg/cm^2). Using Equation 9, the parameter estimates were f = -0.61 and h = 0.35 µm for 50 µg/cm^2 and f = -0.67 and h = 0.41µm for 100 µg/cm^2).

3.2.6 *AMMONIUM NITRATE ON PAINTED ROUGH ALUMINUM*

Ammonium nitrate on painted aluminum was very challenging. As with potassium chlorate, we analyzed the data in two ways: (a) assuming Fresnel reflectance ρ_0, and (b) using an auxiliary reflectance measurement from the integrating sphere as ρ_0. The results are shown in Figure 23. Unlike the potassium chlorate case, there are no evident features associated with the target, and the model produces poor fits to the data.
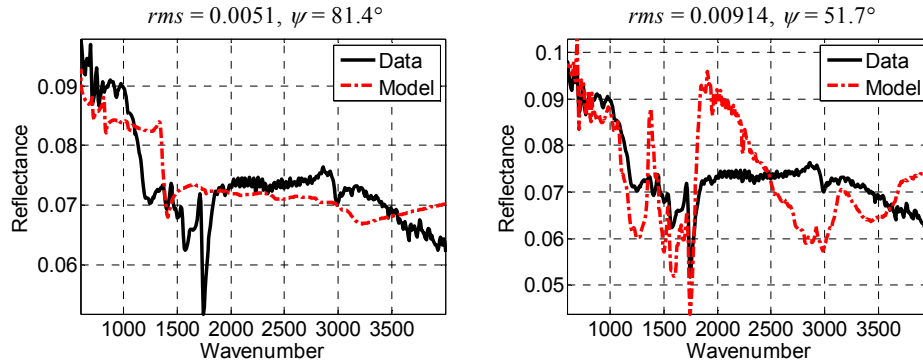
Figure 23. Model results (data in solid black, model in dashed red) applied to specular reflection measurements of ammonium nitrate deposited on painted aluminum at 100 µg/cm^2. *Left*: assuming no knowledge about the substrate (ρ_0 assumed to be 1). *Right*: using an auxiliary measurement of the substrate reflectance.

To shed more light on the situation, we fit the model (using the auxiliary measurement of ρ_0) forcing the f, h, and g parameters to be zero, i.e., it was assumed that no ammonium nitrate was actually present. Figure 24 (top plot) shows this result, where the wavenumber range was limited to wavenumbers less than 1800 cm^{-1} (this was the region where we observed the measured ρ_0 to allow a very good fit for the potassium chlorate data, see Figure 21. Here, the model fit is good, with some slight discrepancies. The bottom plot of Figure 24 shows the residual between the model and the data (red).

36
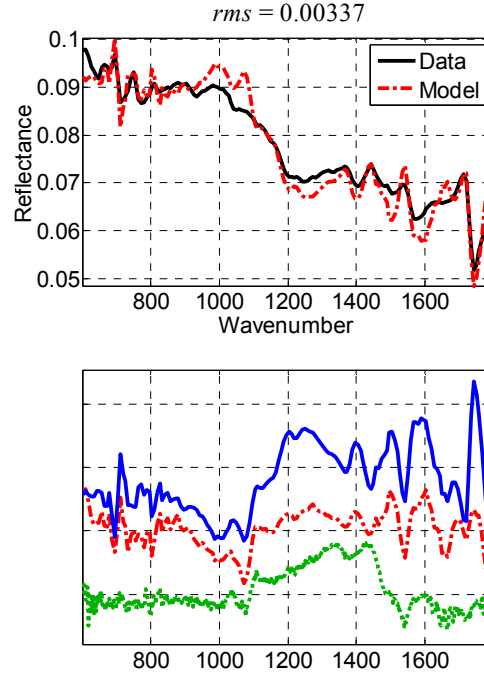
Figure 24. Model results to ammonium nitrate at 100 μg/cm^2 on painted aluminum when it is assumed that no ammonium nitrate is present (i.e., *f, h, g* are forced to equal 0) and knowledge about the substrate is used. *Top*: model results (dashed red) fit the data (black) well, with some slight discrepancies. *Bottom*: model residual (dashed red) is plotted along with ρ_0 (solid blue) and an experimentally determined relative-reflectance spectrum of ammonium nitrate on painted aluminum (dotted green, see text).

The curves are shown in arbitrary units, offset and scaled for comparison purposes. The residual looks almost identical to the ρ_0 spectrum, but there is correlation between the ammonium nitrate spectral shape and the painted aluminum substrate. If the ammonium nitrate is actually present, then we would expect the residual to show a trace of the ammonium nitrate spectral shape. However, the residual looks similar to the reflectance of the painted aluminum. This indicates, perhaps, that the model is unable to perfectly model the substrate reflectance using the measured ρ_0 and the decay term. However, we can also compare to the observed reflectance of the sample as measured in the integrating sphere, where we ratio to a bare painted aluminum reflectance spectrum measured in the integrating sphere. The result is a relative reflectance due to the ammonium nitrate alone (shown in green). Clearly, there are spectral features in common between the ammonium nitrate and the painted aluminum substrate. We believe that this correlation between spectral features is the source of the difficulty in analyzing the ammonium nitrate/painted aluminum samples (a similar problem affects potassium chlorate on a polymer-coated aluminum in the field data, see Section 4.2.2). The presence of ammonium nitrate in the data might be encoded in the peak around 1070 cm^{-1}: in the residual, the peak around 1070 cm^{-1} looks more intense in comparison to the peak at 1000 cm^{-1} than in the ρ_0 spectral shape; there is a peak in the ammonium nitrate spectrum at this location that could account for this difference.

4.   RADIATIVE TRANSFER FOR A TARGET ON ROUGH SUBSTRATE IN FIELD EXPERIMENT

Our objective is to explain the open atmosphere field measurements of contaminated rough surfaces by passive longwave infrared hyperspectral imagers with a simple radiative transfer model. We leverage on our observation that the rough surface reflectance $R_0(\theta)$ has a relatively narrow angular distribution ($\sim \pm 5°$ around the specular direction) for our rough aluminum measurements. We speculate that though in the field the contaminated surface is illuminated by a diffuse downwelling atmospheric radiance, the most dominant contribution to the field measurements is in the specular direction. Thus, we can adopt a one-dimensional (1D) approach where we consider only the input radiance, *L*, along the specular line-of-sight (LOS). This is equivalent to saying that the diffuse radiation field can be represented by some effective input radiance along the LOS (similar to the concept of the diffusivity factor[30]). Therefore, the field model is always a specular model, with $\theta_i = \theta$. In our particular field measurements, the angle *θ* was 45°, with the specular input radiance coming from the zenith.

4.1   THEORY

Let the target have transmission *t* and reflectivity R_t, hence, the target's emissivity is $\varepsilon = 1 - R_t - t$. Let the rough surface have reflectance R_0 and a zero transmission, hence the surface emissivity is $\varepsilon_0 = 1 - R_0$. In the most general case, the temperature, *T*, of the target, and the temperature, T_0, of the substrate are allowed to be different. In the following, the Planck radiation curve associated with a blackbody at temperature *T* will be denoted *B*(*T*).

The radiative transfer for such a system is given with a linear mixture model (Equation 1) by:

$$\left.\begin{cases} M = (1-f) \times [\varepsilon_0 B(T_0) + L \times R_0] + f \times [\varepsilon B(T)R_0 t + \varepsilon B(T) + \varepsilon_0 B(T_0)t + (1-R_t)LR_0 t^2 + LR_t] \\ \varepsilon = 1 - R_t - t \\ \varepsilon_0 = 1 - R_0 \end{cases}\right\} \quad (11)$$

where the first term, $(1-f) \times [\varepsilon_0 B(T_0) + L \times R_0]$, contains the thermal self-emission of the surface, $\varepsilon_0 B(T_0)$, and the atmospheric downwelling radiance reflected by the uncontaminated portions of the surface, $L \times R_0$. Note that for an opaque surface ($t_0 = 0$), $\varepsilon_0 B(T_0) + L \times R_0 = B(T_0) + R_0 \times [L - B(T_0)]$ is a function of the thermal contrast, $L - B(T_0)$. The second term in the mixture model includes the following contributions: $\varepsilon B(T)R_0 t$ is the target's self-emission that is reflected by the rough surface and transmitted through the target; $\varepsilon B(T)$ is the target self-emission; $\varepsilon_0 B(T_0)t$ is the surface self-emission transmitted through the target; $(1-R_t)LR_0 t^2$ is the downwelling radiance reflected by the surface and attenuated by the target (two way transmission); and LR_t is the downwelling sky radiance reflected by the target. This model assumes that the contaminated surface is close to the sensor (i.e., the stand-off distance is small), since there is no intervening atmospheric transmission between the sensor and the contaminated surface appearing in the model, and multiple reflections between the target layer and the underlying surface are also neglected.

The substrate and target are potentially rough surfaces, and therefore the reflectivity terms R_t and R_0 are modeled using the decay model (Equation 3, Section 2.1.1) with roughness coefficients (a_t, b_t, c_t) and (a_0, b_0, c_0), respectively. The target's transmission is modeled in the same way as Section 3.1.1. The effective source radiance, L, is an unknown spectral vector and must be estimated from the data or by some other means. To account for the fact that L is an estimated quantity, and may not be absolutely correct, we add a gain and offset parameters to the model, so that $L \rightarrow l_1 L + l_2$. Therefore, the full field model is achieved by substituting Equation 12 into Equation 11.

$$\left\{ \begin{array}{l} R_0 = \rho_0 \exp(a_0 \lambda^{-2} + b_0 \lambda^{-1} + c_0) \\ R_t = \rho_t \exp(a_t \lambda^{-2} + b_t \lambda^{-1} + c_t) \\ t^2 = \exp\left(-2h(\alpha + g\Delta n)/\cos\theta\right) \\ L \rightarrow l_1 \times L + l_2 \end{array} \right\} \tag{12}$$

The full model has 13 unknowns $(f, h, g, a_0, b_0, c_0, T_0, a_t, b_t, c_t, T, l_1, l_2)$. Note that using the decay model for the reflectivities of the target and underlying surface impacts the emissivities $(\varepsilon_s, \varepsilon)$ in Equation 11. We note that computing emissivity from directional reflectance is correct because the general form of Kirchhoff's law (reference 10, Equation 3-12) states that under thermodynamic equilibrium a detailed radiative balance should be maintained between absorption and emission for both angle and wavelength, $\varepsilon(\lambda, \theta) = absorption(\lambda, \theta)$. Hence, for an opaque body we can write $\varepsilon_0(\lambda, \theta) = 1 - R_0(\lambda, \theta)$. We can follow the same solution process as described in 3.1.3, however, as with the lab model, the numerical procedure can benefit from a fewer number of parameters. Thus, there are several simplifications of Equations 11 and 12 that should be considered.

First, as is done with the lab model, the surface reflectance from the target may be neglected, eliminating the (a_t, b_t, c_t) parameters. Secondly, it is possible that the material and surface temperatures will equilibrate to the same value, $T = T_0$. These two simplifications result in a simpler form of the model,

$$M = B(T_0) + R_0\left(L - B(T_0)\right) \times \left[1 - f + ft^2\right] \tag{13}$$

with only 9 parameters, $\eta = (f, h, g, T_0, a_0, b_0, c_0, l_1, l_2)$. This is the form that we implemented and used in the results Section 4.2.2. Furthermore, we observe in the results (Section 4.2.2) that we achieve a good fit in the model extracting L from a diffuse gold panel (visible in the hyperspectral imagery) where the solution values of l_1 and l_2 are close to 1 and 0, respectively. This is an indication that the estimated L from the diffuse gold is a good estimate for the model, and thus it may be possible to remove the l_1 and l_2 parameters. This would result in a model with only 7 parameters, which is slightly more complicated than Equation 9.

It can be shown that the field model (Equation 11) reduces to the lab models (Equations 9 and 10), depending on whether R_t is neglected). Divide Equation 11 by the source radiance L to convert to reflectance, R, and assume that the source intensity $L >> B(T)$ and $L >> B(T_0)$, hence, self-emissions from the surface and the target are negligible. For example,

$\dfrac{M}{L}\,Eq.(13)\xrightarrow{\ L>>B\ } R\ Eq.(9)$. The equivalent brightness temperature of the external source used in the lab experiment is on the order of a thousand Kelvin or more, whereas ambient lab temperature is ~300K.

4.2   RESULTS

In this section we show results analyzing field data, where potassium chlorate was deposited on one of two types of substrates, and placed 10 *m* away from a passive LWIR hyperspectral sensor. The sensor collected 17 sequential data cubes in time, which were averaged in order to increase the signal to noise ratio. Section 4.2.1 shows results from a black, non-reflective material. Section 4.2.2 shows results from aluminum that, unfortunately, was coated with an unknown polymer. This reduced the correspondence to the samples measured in the lab on rough aluminum (Section 3.2). Additionally, the polymer and potassium chlorate spectral shapes correlate, further complicating the analysis. The same error metrics described in Section 3.2 (*rms* error and matching angle *ψ*) are used in this section to judge the quality of the fits.

4.2.1   *POTASSIUM CHLORATE ON BLACK SURFACE*

The black material in the hyperspectral imagery was mostly featureless, and appeared similar to a Planck blackbody spectrum at 329 K. Assuming that the opaque black material was actually a blackbody with emissivity ε_0 = 1 allowed for a convenient simplification of Equation 11. In this case, there is no need to model an input radiance (since ε_0 = 1 implies R_0 = 0), and the model reduces to $M = B(T_0) + f \times \Delta T \times [t-1]$ where $\Delta T = B(T_0) - B(T)$ and t is the one-way transmission of photons emitted from the substrate through the target layer. The results, in Figure 25, are shown in brightness temperature in order to remove the slope associated with the Planck blackbody curve. Absorption coefficients from the KBr pellet method were used in the model. There is some lack of fit that may suggest the model was over simplified, however, even the simplified model provides a good fit.
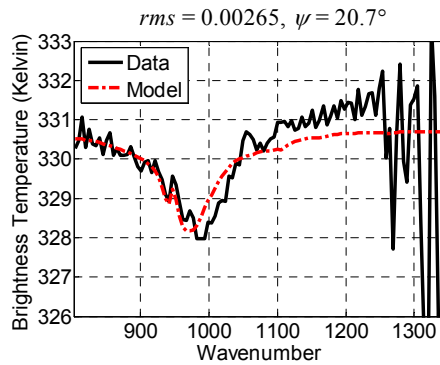
Figure 25. Model results applied to field measurements of potassium chlorate deposited on a black (non-reflective) substrate, using α_{pellet}.

4.2.2   *POTASSIUM CHLORATE ON ROUGH ALUMINUM*

The rough aluminum substrate considered in the field was not the same substrate as considered in the lab. The intention was that information we learned and conclusions we made regarding rough aluminum in the lab would be able to be validated using the field

measurements. However, an unknown transparent polymer coating covered the aluminum used in the field. This reduced the correspondence between the lab and field scenarios, and of course, the field is additionally complicated by more complex radiometry due to diffuse atmospheric radiance that does not occur in the lab. In order to apply the model to the field data, we used an auxiliary reflectance measurement of the bare coated aluminum surface. We have already shown in Section 3.2.5 that auxiliary reflectance measurements can be used successfully to represent spectral features due to the substrate. The input radiance, L, needed for our model was taken from a diffuse gold panel that was placed in the scene. The field model includes gain and offset parameters l_1 and l_2 that allow modifying the input radiance in case it is a poor estimate; however, in all cases $l_1 \cong 1$ and $l_2 \cong 0$, indicating that the diffuse gold panel provides a good estimate of the effective LOS radiance input on the samples.

Figure 26 shows results of the model. In the left plot, the data comes from an area in the image where the coated aluminum is not contaminated with potassium chlorate (the H_0 condition). The model result (dashed green) is found using Equation 13 but fixing target parameters f, h, and g to zero. The good quality of the fit indicates that the one-dimensional representation of the diffuse input radiance and the auxiliary measurement of the reflectance from the coated aluminum substrate are successful in modeling the H_0 radiance. In the right plot, the data are from an area of the image where the coated aluminum is contaminated with potassium chlorate (the H_1 scenario). Two model curves are shown in each plot. The red dashed curve is an unconstrained fit, where the model will increase (or decrease) all 9 parameters in Equation 13 in order to improve the fit. The green dotted curve is constrained such that those parameters associated with the target are forced to be zero (i.e., $f = h = g = 0$). For both the H_0 and H_1 data the two fits are essentially identical! Thus, although the model successfully fits field radiance from contaminated and uncontaminated coated aluminum, the model apparently cannot detect or identify the presence of potassium chlorate in this instance. Although the model can successfully represent field radiance from both contaminated and uncontaminated coated aluminum, the model is unable to detect or identify the presence of potassium chlorate.
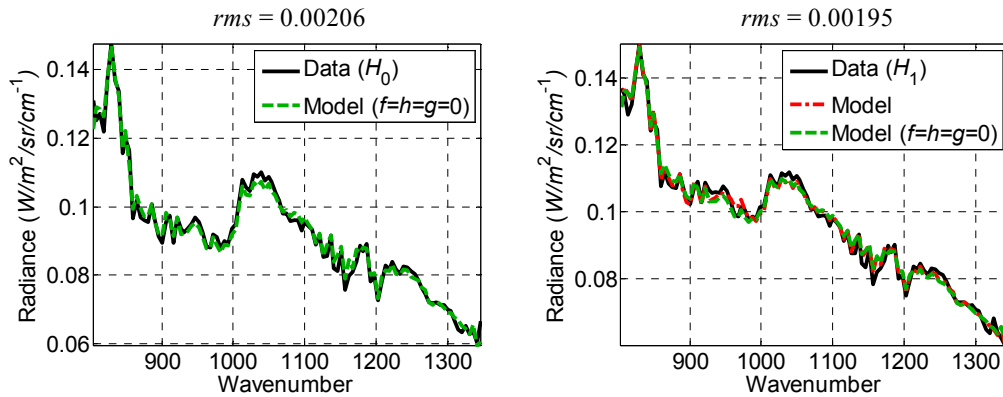
Figure 26. Model results applied to field measurements of potassium chlorate on a coated aluminum substrate, using α_{pellet}. _Left_: H_0 data (potassium chlorate is absent; black) fit with Equation 13, where target parameters f, h, and g are constrained to equal 0 (dashed green). _Right_: H_1 data (potassium chlorate is present; black) is shown along with two model fits: unconstrained (red) and constrained such that $f = g = h = 0$ (dashed green).

To shed light on the issue, we took the ratio of the H_1 spectrum to the H_0 spectrum, to create a relative reflectance spectrum. The H_0 and H_1 spectra are shown in the top plot of

Figure 27, and there is a clear difference in the magnitude of the radiance over the 800-1000 cm^{-1} range. The relative reflectance spectrum, H_0/H_1, is shown in black in the bottom plot in Figure 27, along with two other curves. The dotted green curve shows the auxiliary reflectance measurement, R_0, of the uncontaminated polymer-coated aluminum substrate (scaled for display purposes).
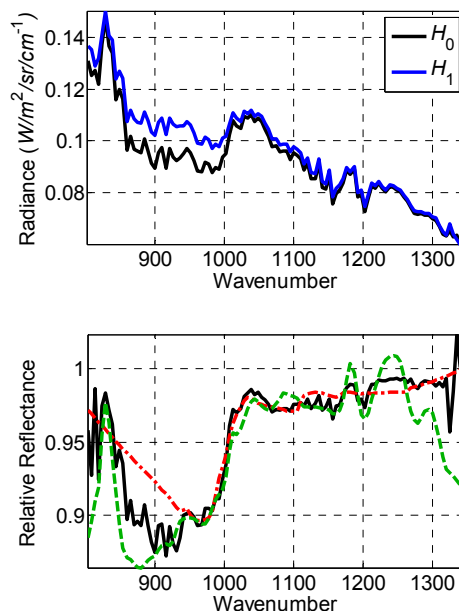
Figure 27. *Top:* H_0 and H_1 radiance shown in blue and black, respectively. *Bottom*: relative reflectance (H_0/H_1, black) is plotted with the auxiliary reflectance measurement of the uncontaminated polymer-coated aluminum substrate (green) and a potassium chlorate spectrum (red) derived from α_{pellet} (a model fit for H_0/H_1 using Equation 9 assuming $R_0 = 1$).

The relative reflectance and the substrate reflectance curves are highly correlated and look very similar. Also shown, in dashed red, is a model fit using α_{pellet} for potassium chlorate, assuming $R_0 = 1$ (in order to determine how well the relative reflectance can be explained by potassium chlorate, only); it is correlated to both the relative reflectance and the substrate reflectance curves. The correlation makes it very difficult to identify the presence of the target, since mathematically the observed spectral shape in the data can be explained by either the substrate or the target. This is similar to the ammonium nitrate on painted aluminum, where there was a correlation between the substrate and the target, and a lack of clear target features in the data (Section 3.2.6).

We also applied Equation 9 directly to the relative reflectance spectrum, using both α_{pellet} and the spectral shape from the substrate reflectance, R_0. Figure 28 shows these results, which show quite a good fit. Again, though, because of the ambiguity caused by the correlation between the substrate and the target features it is unclear if these results could be used for reliable detection/identification of potassium chlorate on this particular substrate. More data and experimentation would be necessary to determine the performance metrics (false alarm rate, detection limits, etc.) of the model.
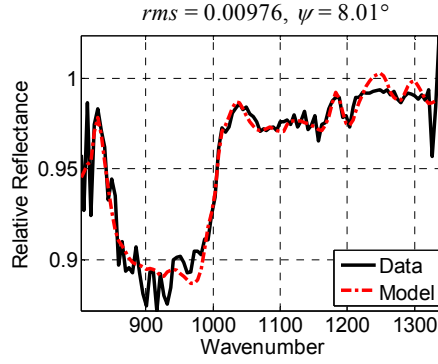
Figure 28. Result of applying the lab model (Equation 9, designed for reflectance) to the relative reflectance spectrum from Figure 27, using α_{pellet} and the residual reflectance shape of the uncontaminated target (the auxiliary reflectance measurement, R_0).

5.   SUMMARY

We developed a radiative transfer framework for measured radiance from contaminated rough surfaces. Formulating a model to explain radiance measurements is a first important step for solving the detection problem. Our framework is a combination of theoretical-based radiative transfer (conservation of energy), an empirical approximation for reflectance of rough surfaces (with the decay function $D(a,b,c)$) and empirical modifications of the target absorption coefficients (the function $g\Delta n$). In our modeling effort we neglect (a) multiple reflections between the target regions and the bare substrate—hence our mixture model, Equation 1, is linear with the fill-factor f—and (b) scattering events within the target's volume (which require knowledge of scattering functions that are dependent on target's particles shape, size and orientation; we decided to avoid these complications). However, we think that the $g\Delta n$ term is related to scattering: this term accounts for variations in pathlength which in turn will correlate with the probability of scattering within the target.

The full form of the radiative (Equation 11) transfer model is a one-dimensional radiative transfer model (i.e., one angle is used in place of the full diffuse radiance field) where the target and the substrate may be at two different temperatures, and emission terms are included (appropriate for field measurements). The full model reduces to a model that explains observed reflectance (specular or off-specular) where the incident radiation is from a strong directional source (Equation 11 → Equation 10), which represents the ellipsometer (lab) measurements. Further simplifications that reduce the number of parameters appearing in the model may be made (e.g., Equation 10 → Equation 9). Since the model is fit through a numerical optimization routine, reducing the number of parameters helps in the solution process. In the simplest model (Equation 9) the unknown parameters are the fill factor, f, target height, h, dispersion factor, g, and roughness coefficients a_0, b_0, c_0. In the analysis of potassium chlorate and ammonium nitrate reflectance measurements collected in the lab, the simpler model (Equation 9) was sufficient.

Although the simplicity of the model makes the numerical optimization procedure comparatively easier, and leaves fewer mathematical degrees of freedom with which to fit arbitrary spectral shapes (i.e., exhibits higher specificity and reduces the danger of overfitting the data), the disadvantage is that if the model is too simple, the solution parameter set may not attain physical values (e.g., $0 < f < 1$ or $h > 0$). This hurts the interpretability of the model, and

raises questions about how to algorithmically conclude that a specific target is present. For example, if the model was perfect, and h was a good estimate of the true material height, then one could simply threshold the value of h to give a detection result. This is not possible if h is non-physical. However, nonphysical values do not necessarily invalidate the results of the model. For example, if the model fits observed spectral features in a measured spectrum by using a signature from a particular material, the conclusion that the material is actually present can still be the correct decision, regardless of the values of the parameter set.

Our radiative transfer model for reflectance (Section 3.1) produced good results (excellent fit between the model and the measurements) for lab measurements (using strong directional incidence) of potassium chlorate on rough aluminum, painted aluminum, and an aluminum mirror; good results were also obtained for ammonium nitrate on rough aluminum. Ammonium nitrate on painted aluminum was more complicated due to a spectral correlation between ammonium nitrate features and spectral features in the polymer-coated painted aluminum.

We observed that most of the signal energy came from the specular direction (high signal-to-noise ratio), very little energy from off-specular (low signal-to-noise ratio). Nevertheless, fits to off-specular reflection were good, though more challenging (especially for potassium chlorate). Because of the highly specular nature of these rough substrates, the ability of the model to explain off-specular reflection is of lower importance. We also observed high specificity with respect to ammonium nitrate and potassium chlorate: in both cases the model failed to fit the data when the wrong material was assumed to be present.

The specular behavior of the substrates also caused us to develop the hypothesis that the diffuse atmospheric radiation field (which is complicated) may not need to be modeled, and that a one-dimensional model propagating the specular LOS radiance (Equation 11) may be sufficient to explain the field-measured radiance. The field data was complicated by the fact that the aluminum substrate in the field was not the same aluminum that we analyzed in the lab (it was coated by a polymer; as with ammonium nitrate on painted aluminum, there was a spectral correlation between the substrate and the target signature). The one-dimensional model successfully predicts the radiance from the uncontaminated and contaminated polymer-coated aluminum; however the correlation complicates the detection decision.

Our model is formulated such that two-way attenuation (by absorption) through the target material is the primary source for spectral features to appear in the observed radiance. Therefore the absorption coefficient, α, is an important input to the model. We deduce the absorption coefficient for the target from integrating sphere transmission measurements of a dilute KBr mixture (pellet). This does not capture the morphology of the material deposition (roughness, irregularities, etc.), but can model the data well; the advantage of the pellet method is that only one reference spectrum per target material is required. However, morphology can be important, and α_{pellet} may result in insufficient model fits. We described an experimental procedure in which to obtain estimates of α that include morphology (Sections 2.1.3 and 2.2.3). This may require more than one reference spectrum (more than one α) per material to cover the different deposition morphologies. One also may need to account for different substrates, since we have empirical evidence that the nature of the underlying substrate will affect the final morphology, even for an identical deposition procedure (compare Figure 11, right plots, with Figure 19, left plots, which have the same deposition of potassium chlorate on a rough versus smooth aluminum surface). Measuring all possible morphologies on all possible substrates is probably not an achievable product.

This study was conducted over a short time (six months) and thus, due to the limited available data (limited lab measurements were conducted during this period) our conclusions and models need to be further verified and tested on larger data sets.

5.1 MAIN INNOVATIONS, IDEAS AND INSIGHTS

- Non-uniformity of the surfaces: we observed that the directional reflectance from brushed aluminum varied greatly as a function of orientation and location. <u>Significance</u>: it may be unrealistic to assume that reliable H_0 (target absent) measurements can be taken from some part of a surface and be used (without modification) in the radiative transfer model.

- A model to describe angular reflectance of a rough surface using an exponential decay term modifying the theoretical Frensel reflectance (Section 2.1.2, Equation 3). This model is an empirical extension of a theoretically based derivation. <u>Significance</u>: This is a first step towards building a model for a *contaminated* rough surface. In addition, we observed that auxiliary H_0 measurements can be substituted for the theoretical Fresnel reflection, and used successfully in the radiative transfer model (the decay term is able to account for some amount of variation).

- A procedure (credited to Barry Williams) for directly measuring intrinsic absorption coefficients without the effect of scattering losses. This method uses transmission measurements through an integrating sphere to detect scattered photons. <u>Significance</u>: the method enables development of a signature library of α coefficients, which is the primary input to the radiative transfer model. Absorption coefficients are rich in spectral information.

- A procedure to measure absorption coefficients that capture the morphology of the target deposition, which is based on calibrating an integrating sphere reflectance measurement to the integrating sphere transmission measurement (see Sections 2.1.3 and 2.2.3). <u>Significance</u>: can improve the signature library by incorporating morphology effects, however, due to different morphologies and depositions, more than one signature per material might be required.

- Non-Lambertian surfaces and the importance of specular angle direction. We observed that for the rough aluminum most of the reflectance (see Section 2.2.1) is in the specular direction. Contaminated rough aluminum samples were also highly specular in nature. <u>Significance</u>: (a) It allows simplifying the radiative transfer model to be based on a two-way attenuated incident radiation, and (b) allows the diffuse radiation field to be ignored. We hypothesize that in field measurements, the best location for the sensor is where the specular ray has the highest thermal contrast (in the case of the longwave IR spectral region) or points to the sun (in the midwave or shortwave IR).

- Modifications of the transmission in an absorbing medium (the target) with the function $g\Delta n$ (see Section 3.1.1). <u>Significance</u>: This empirically-motivated modification accounts for variations in pathlength in the target medium as a function of wavelength; we hypothesize that this term may implicitly account for some volume scattering that does not explicitly appear in our model (since the probability of scattering is related to the path through the material).

- Deeper spectral signatures were observed for specular reflectance measurements of potassium chlorate on rough aluminum as the incident angle became smaller (closer to normal). Significance: In operational scenarios it may be beneficial to set up the measurement geometry using a small incident angle.

5.2   OPEN QUESTIONS

- In this study we studied only a few samples. Thus, the validity of our model and observation need to be further studied and verified.

- How well our rough surface reflectance model (the decay model) work on other surfaces (e.g., dielectric materials such as wood and soils)?

- Can the empirical coefficients (a, b, c) in the decay function (Equation 3) can be expressed as a function of roughness properties?

- Can we provide a solid physical explanation for our $g\Delta n$ function and for the second order polynomial in the decay function $D(a, b, c)$? Our explanation of the two is not rigorous.

- Why is capturing the morphology of the potassium chlorate deposition (using α instead of α_{pellet}) important, whereas for ammonium nitrate it is not?

- Why is there a qualitative difference in the behavior of off-specular reflectance between potassium chlorate and ammonium nitrate (for ammonium nitrate the specular shape for off-specular and specular are similar; for potassium chlorate there is a polarity change).

5.3   FUTURE RESEARCH

- Explore the implications of our radiative transfer model on signal processing detection algorithms. Evaluate the performance of the model in detecting and identifying different targets.

- Improve the physical radiative transfer model by including multiple reflections between the target and underlying surface, in the hope that a more accurate model will reduce the mathematical non-uniqueness of the solution and reduce the likelihood of non-physical solution values (e.g., negative h and $f > 1$).

- Improve the numerical optimization routine (the Newton-Raphson method) for improved robustness.

- Conduct more lab measurements on different contaminated rough surfaces (different surfaces and targets).

6.   RECOMMENDATIONS

Our radiative transfer model produced good results in the lab where an active directional radiation source (ellipsometer) was used and reflectance was measured at the specular direction. Develop a hand-held field sensor with its own source and a specular collection

geometry (is there a particular incidence angle that is optimal?). This may enable identification of ammonium nitrate in the LWIR region, since the atmospheric transmission window will have no impact over very short stand-off distances.

Model results applied to field data for as aluminum substrate were inconclusive. There were too many differences between the lab measurements and the field scenario that prevented translating conclusions made in the lab to the field. We recommend repeating the field test in a more controlled fashion. In addition, obtain angularly resolved spectral measurements of the atmospheric downwelling radiance to verify the importance of the specular direction.

7. LITERATURE CITED

1. C. Asmail, (1991). "Bidirectional scattering distribution function (BSDF): a systematized bibliography," *J. Res. Natl. Inst. Stand. Technol.*, 96, p215-223.

2. G. T. Ruck, D. E. Barrick, W. D. Stuart, and C. K. Krichbaum, (1970). *Radar cross-section handbook*, Vol. 1, Plenum Press: New York, NY.

3. F. T. Ulaby, R. Moore, and A. K. Fung, (1986). *Microwave remote sensing active and passive*, Vol. II, Artech House: Norwood, MA.

4. J. A. Ogilvy, (1991). *Theory of wave scattering from random rough surfaces*, Institute of Physics Publishing: Philadelphia, PA.

5. B. Hapke, (1993). *Theory of reflectance and emittance spectroscopy*, Cambridge University Press.

6. J. M. Bennett and L. Mattsson, (1999). *Introduction to surface roughness and scattering*, 2nd edition , Optical society of America: Washington, D.C.

7. S. M. Kay, (1998). *Fundamentals of statistical signal processing, Detection theory*, Prentice Hall PTR: Upper Saddle River, NJ.

8. M. J. Kavaya, R. T. Menzies, D. A. Haner, U. P. Oppenheim, and P. H. Flamant, (1983). "Target reflectance measurements for calibration of lidar atmospheric backscatter data," *Appl. Opt.*, 22, p2619-2628.

9. D. A. Haner and R. T. Menzies, (1989). "Reflectance characteristics of reference materials used in lidar hard target calibration," *Appl. Opt.*, 28, p857-864.

10. R. Siegel and J. R. Howell, (1992). *Thermal radiation heat transfer*, 3rd edition, Taylor & Francis.

11. C. Baylard, J. J. Greffet, and A. M. Maradudin, (1993). "Coherent reflection factor of a random rough surface: applications," *J. Opt. Soc. Am. A.*, 10, p2637-2647.

12. M. Born and E. Wolf, (1980). *Principles of optics*, 6th edition, Pergamon Press: New York, NY.

13. A. Rakic, (1995). "Algorithm for the determination of intrinsic optical constants of metal films: application to aluminum", *Appl. Opt.*, 34, p4755-4767.

14. P. K. Cheo and J. Renau, (1969). "Wavelength dependence of total and depolarized back-scattered laser light from rough metallic surfaces," *J. Opt. Soc. Am. A.,* 59, p821-826.

15. Katz, (1966). "Wavelength dependence of the radar reflectivity of earth and moon," *J. Geophys. Res.* 71, p361-366.

16. L.M. Spetner and I. Katz, (1960). "Two statistical models for radar terrain return," *IEEE Trans. Antennas Propagation*, AP-8, p242-246.

17. L. J. Battan, (1973). *Radar observation of the atmosphere*, University of Chicago Press: Chicago, IL.

18. C. F. Bohren and D. R. Huffman, (1983). *Absorption and scattering of light by small particles*, Wiley: New York, NY.

19. H. C. van de Hulst, (1981). *Light Scattering by Small Particles*, Dover Publications, New York.

20. K. N. Liu, (2002). *An introduction to atmospheric radiation*, 2nd edition, Academic Press: New York, NY.

21. K. E. Torrance and E. M, Sparrow, (1967). "Theory for off-specular reflection from roughed surfaces," JOSA, 57, p1105-1114.

22. M. A. Jarzembski, M. L. Norman, K. A. Fuller, V. Srivastava, and D. R. Cutten, (2003). "Complex refractive index of ammonium nitrate in the 2-20-um spectral range," *Appl. Opt.*, 42 (6), p922-930.

23. G. R. Fowles, (1989). *Introduction to Modern Optics*, 2nd edition, Dover Publications: New York.

24. S. A. Kovalenko, (2001). "Descartes-Snell law of refraction with absorption," Semiconductor Physics, Quantum Electronics and Optoelectronics, 4 (3), p214-218.

25. P. Yang and K. N. Liu, (1995). "Light scattering by hexagonal ice crystals: comparison of finite-difference time domain and geometric optics models," *J. Opt. Soc. Am. A.*, 12, p162-176.

26. J. S. Toll, (1956). "Causality and the dispersion relation: logical foundations," *Phys. Rev.*, 104, p1760-1770. [see also: Lecture 21 by Lucas Illing of Reed College, Portland, OR. http://academic.reed.edu/physics/courses/Physics323.s09/lec.html]

27. R. W. Hamming, (1973). *Numerical Methods for Scientists and Engineers*, McGraw-Hill: New York, NY.

28. F. S. Acton, (1990). *Numerical Methods that Work*, Mathematical Association of America: Washington, DC.

29. http://www.mathworks.com/help/techdoc/ref/fminsearch.html

30. W. M. Elsasser, (1942). *Heat Transfer by Infrared Radiation in the Atmosphere*, Harvard Meteorological Studies (Harvard U. Press), Vol. 6, p107.
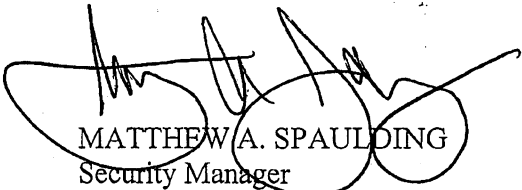
REPLY TO
ATTENTION OF

RDCB-DPS-RS

AUG 2 7 2014

MEMORANDUM THRU Director, Edgewood Chemical Biological Center, (RDCB-D/Mr. Joseph Wienand), 5183 Blackhawk Road, Aberdeen Proving Ground, Maryland 21010-5424

FOR Defense Technical Information Center, 8725 John J. Kingman Road, Ft Belvoir, VA 22060

SUBJECT: Internal Request for Change in Distribution

1. This action is in response to an Edgewood Chemical Biological Center (ECBC) Internal Request for a Change in Classification and Distribution on ECBC Technical Report 1084 the "Radiative Transfer Model for Contaminated Rough Surfaces." This document was authored by Ben-David, Avishai and Davidson, Charles E." and is currently Unclassified – For Official Use Only (FOUO) with a distribution authorized to US Government Agencies and their contractors only.

2. The above listed document has been reviewed by two ECBC Subject Matter Experts and deemed suitable for the change in distribution to read "Distribution Statement A – Approved for Public Release, Distribution Unlimited."

3. The point of contact is Mr. Ronald L. Stafford, ECBC Security Specialist, (410) 436-6810 or ronald.l.stafford.civ@mail.mil.

MATTHEW A. SPAULDING
Security Manager